AGU PUBLICATIONS

JGR

Journal of Geophysical Research: Solid Earth

RESEARCH ARTICLE
10.1002/2013JB010328

Key Points:
- Peridotite pyroxenes provide constraints on upper mantle water variations
- Water in olivine is calculated from water in pyroxene and partition coefficients
- Peridotites are relatively water rich for the residues of partial melting

Supporting Information:
- Readme
- Table S1
- Table S2
- Table S3
- Table S4

Correspondence to:
J. M. Warren,
warrenj@stanford.edu

Citation:
Warren, J. M., and E. H. Hauri (2014), Pyroxenes as tracers of mantle water variations, *J. Geophys. Res. Solid Earth*, *119*, 1851–1881, doi:10.1002/2013JB010328.

Received 30 APR 2013
Accepted 26 FEB 2014
Accepted article online 4 MAR 2014
Published online 28 MAR 2014

Pyroxenes as tracers of mantle water variations

Jessica M. Warren[1] and Erik H. Hauri[2]

[1]Department of Geological and Environmental Sciences, Stanford University, Stanford, California, USA, [2]Department of Terrestrial Magnetism, Carnegie Institution of Washington, Washington, DC, USA

Abstract The concentration and distribution of volatiles in the Earth's mantle influence properties such as melting temperature, conductivity, and viscosity. To constrain upper mantle water content, concentrations of H_2O, P, and F were measured in olivine, orthopyroxene, and clinopyroxene in mantle peridotites by secondary ion mass spectrometry. Analyzed peridotites are xenoliths (Pali Aike, Spitsbergen, Samoa), orogenic peridotites (Josephine Peridotite), and abyssal peridotites (Gakkel Ridge, Southwest Indian Ridge, Tonga Trench). The comparison of fresh and altered peridotites demonstrates that low to moderate levels of alteration do not affect H_2O concentrations, in agreement with mineral diffusion data. Olivines have diffusively lost water during emplacement, as demonstrated by disequilibrium between olivine and coexisting pyroxenes. In contrast, clinopyroxene and orthopyroxene preserve their high-temperature water contents, and their partitioning agrees with published experiments and other xenoliths. Hence, olivine water concentrations can be determined from pyroxene concentrations using mineral-mineral partition coefficients. Clinopyroxenes have 60–670 ppm H_2O, while orthopyroxenes have 10–300 ppm, which gives calculated olivine concentrations of 8–34 ppm. The highest olivine water concentration translates to an effective viscosity of 6×10^{19} Pa s at 1250°C and ~15 km depth, compared to a dry effective viscosity of 2.5×10^{21} Pa s. Bulk rock water concentrations, calculated using mineral modes, are 20–220 ppm and correlate with peridotite indices of melt depletion. However, trace element melt modeling indicates that peridotites have too much water relative to their rare earth element concentrations, which may be explained by late-stage melt addition, during which only hydrogen diffuses fast enough for reequilibration.

1. Introduction

The presence of water in the Earth's mantle affects many of its properties, from the depth of melting to the rheology of minerals. In the upper mantle, water is hosted in all the main mineral phases (olivine, orthopyroxene, clinopyroxene, and garnet) of peridotite. These minerals are referred to as nominally anhydrous minerals (NAMs) as they do not contain hydrous groups in their formulas. Nonetheless, the presence of trace amounts of water reduces mantle viscosity by 2 to 3 orders of magnitude and results in the onset of melting tens of kilometers deeper than in dry mantle [*Hirth and Kohlstedt*, 1996]. Water in olivine has also been shown to change the principle slip system for olivine during dislocation creep [*Jung and Karato*, 2001], the dominant mechanism by which flow in the uppermost mantle occurs.

Traditionally, analysis of water has been done by Fourier transform infrared spectroscopy (FTIR) [e.g., *Bell and Rossman*, 1992]. Analysis by FTIR requires oriented crystals with at least two polished surfaces [e.g., *Bell et al.*, 2003], which is difficult for small grains. In addition, there has been much debate regarding the interpretation of OH stretching bands and the conversion of complex absorption spectra into water concentrations [e.g., *Bell et al.*, 2003; *Aubaud et al.*, 2009; *Kovács et al.*, 2010; *Stalder et al.*, 2012; *Mosenfelder and Rossman*, 2013a, 2013b; *Withers*, 2013].

Recently, analysis of NAMs using secondary ion mass spectrometry (SIMS) has become routine, due to technique development and availability of mineral standards [*Koga et al.*, 2003; *Hauri et al.*, 2006; *Aubaud et al.*, 2007; *Mosenfelder et al.*, 2011; *Withers et al.*, 2012; *Mosenfelder and Rossman*, 2013a, 2013b]. SIMS has the advantage over FTIR in that the analysis is not dependent on mineral orientation and only one polished crystal surface is required. However, the detection limit for water by SIMS is generally higher than by FTIR, due to background water concentrations and detector sensitivity. Also, the majority of SIMS olivine standards have been calibrated by FTIR and thus are subject to the same uncertainties as FTIR data [*Koga et al.*, 2003; *Aubaud et al.*, 2007], though recent work has cross-calibrated olivine standards with other techniques [*Aubaud et al.*, 2009; *Mosenfelder et al.*, 2011; *Withers et al.*, 2012]. In contrast, orthopyroxene and

clinopyroxene have higher water concentrations [*Bell and Rossman*, 1992; *Ingrin and Skogby*, 2000; *Demouchy et al*., 2006; *Grant et al*., 2006, 2007a, 2007b; *Hauri et al*., 2006; *Kohn and Grant*, 2006; *Skogby*, 2006; *Withers and Hirschmann*, 2007; *Tenner et al*., 2009, 2012; *Peslier*, 2010; *Ardia et al*., 2012] and less uncertainty exists with respect to pyroxene standard calibrations [*Koga et al*., 2003; *Aubaud et al*., 2007; *Mosenfelder and Rossman*, 2013a, 2013b].

The majority of previous peridotite water concentration analyses have been in NAMs from continental xenoliths and a few oceanic xenoliths (see *Peslier* [2010] for a review). Water concentrations in abyssal peridotites have only been measured in three previous studies [*Gose et al*., 2009; *Peslier*, 2010; *Schmädicke et al*., 2011] and no data for orogenic or ophiolitic peridotites are reported in the literature. Abyssal peridotites refer to samples collected on the seafloor either at mid-ocean ridges or in subduction zones. They are depleted residues of the melting that forms oceanic crust and typically have lower trace element concentrations than peridotite xenoliths from continental lithosphere. Ophiolitic and orogenic peridotites refer to obducted pieces of oceanic lithosphere—with or without the overlying crust—that typically are from suprasubduction zone settings.

The lack of water measurements in abyssal, orogenic, and ophiolitic peridotites is due to (i) concerns about the effects of alteration, mainly due to the formation of serpentine, and (ii) concerns about diffusive loss of water during ascent to the surface. In xenoliths, olivine typically looses water during ascent to the surface, as H^+ diffuses rapidly in this mineral [e.g., *Kohlstedt and Mackwell*, 1998]. The general exceptions are kimberlite xenoliths, which are brought rapidly to the surface from very deep and sometimes preserve their original water concentrations [*Demouchy et al*., 2006; *Peslier et al*., 2008, 2012]. In contrast, abyssal and orogenic peridotites are emplaced at plate spreading rates (i.e., emplacement timescales are much slower compared to xenoliths), but tectonically exposed peridotite massifs are also ~6 orders of magnitude larger in size than xenoliths.

In this paper, we use SIMS to measure water concentrations in olivine, orthopyroxene, and clinopyroxene from a variety of peridotites, with a focus on the oceanic mantle. Samples include abyssal peridotites from the Gakkel Ridge, Southwest Indian Ridge, and Tonga Trench; xenoliths from Pali Aike, Spitsbergen, and Samoa; and orogenic peridotites from the Josephine Peridotite. We demonstrate that olivine in all samples has lost water but that orthopyroxene and clinopyroxene maintain their high temperature water concentrations. Except at very high degrees of alteration, hydrothermal processes do not affect mineral water concentrations.

2. Geologic Setting of Samples

Peridotites investigated encompass xenoliths, orogenic peridotites, and abyssal peridotites (Table 1). All xenoliths are fresh, while orogenic samples from the Josephine Peridotite have low degrees of serpentinization and abyssal peridotites range from fresh to highly altered. Continental xenoliths are from Pali Aike, Patagonia, [*Stern et al*., 1989, 1999] and Sverrefjell, Spitsbergen [*Amundsen et al*., 1987; *Ionov et al*., 1993, 1996], while oceanic xenoliths are from Savai'i, Samoa [*Hauri et al*., 1993; *Hauri and Hart*, 1994]. Carbonatite metasomatism has been documented in xenoliths from Spitsbergen and Samoa, including a Samoa sample in this study (SAV-1-28). Orogenic samples are from shear zones in the Josephine Peridotite, Oregon [*Kelemen and Dick*, 1995; *Warren et al*., 2008], for which water content variations are expected based on changes in olivine lattice-preferred orientations [*Skemer et al*., 2010].

Abyssal peridotites are from the Gakkel Ridge [*Michael et al*., 2003], the Southwest Indian Ridge (SWIR) [*Standish et al*., 2008; *Warren et al*., 2009], and the Tonga Trench [*Fisher and Engel*, 1969; *Wright et al*., 2000]. Gakkel and Tonga samples are unaltered (Figure 1) and were specifically included to provide a comparison to altered abyssal peridotites. In contrast, SWIR samples have moderate to high degrees of alteration (Figure 1) but are well described in terms of major and trace elements, as well as Nd and Sr isotopic compositions [*Warren et al*., 2009].

3. Methods

Twenty-two olivines, 62 orthopyroxenes, and 42 clinopyroxenes were hand picked from 31 peridotites. Grains were mounted in size order from largest to smallest by pressing into indium contained in 1 in. diameter aluminum disks [*Koga et al*., 2003; *Aubaud et al*., 2007]. Grinding on SiC grits exposed the approximate center

Table 1. Sample Locations and Types

Sample	Location	Lithology	Alteration	Phases Analyzed
		Abyssal Peridotites		
PS86-6-38	SWIR, −52.35°S, 13.13°E	Lherzolite	Moderate	Opx, Cpx
Van7-85-30	SWIR, −52.25°S, 15.23°E	Harzburgite	High	Opx
Van7-85-42	SWIR, −52.25°S, 15.23°E	Lherzolite	Moderate	Opx, Cpx
Van7-85-47	SWIR, −52.25°S, 15.23°E	Lherzolite	Moderate	Opx, Cpx
Van7-85-49	SWIR, −52.25°S, 15.23°E	Lherzolite	Moderate	Opx, Cpx
Van7-86-27	SWIR, −52.13°S, 15.15°E	Lherzolite	High	Cpx
Van7-96-09V	SWIR, −53.14°S, 9.98°E	Pyroxenite Vein	Low	Opx, Cpx
Van7-96-16V	SWIR, −53.14°S, 9.98°E	Pyroxenite Vein	Moderate/High	Opx, Cpx
Van7-96-18M	SWIR, −53.14°S, 9.98°E	Perid w/ Pyx Vn	Moderate	Opx
Van7-96-18V	SWIR, −53.14°S, 9.98°E	Pyx Vn in Perid	Moderate	Opx, Cpx
Van7-96-21M	SWIR, −53.14°S, 9.98°E	Harz w/ Pyx Vn	Moderate	Opx, Cpx
Van7-96-21V	SWIR, −53.14°S, 9.98°E	Pyx Vn in Harz	Moderate	Opx, Cpx
Van7-96-25	SWIR, −53.14°S, 9.98°E	Lherzolite	Moderate	Opx, Cpx
Van7-96-28	SWIR, −53.14°S, 9.98°E	Lherzolite	Moderate	Opx, Cpx
Van7-96-35	SWIR, −53.14°S, 9.98°E	Lherzolite	Moderate	Opx, Cpx
Van7-96-38	SWIR, −53.14°S, 9.98°E	Lherzolite	Moderate	Opx, Cpx
HLY0102-40-81	Gakkel Ridge, 85.45°N, 14.56°E	Harzburgite	Fresh	Oliv, Opx
PS59-235-17	Gakkel Ridge, 84.66°N, 4.20°E	Lherzolite	Fresh	Opx, Cpx
7TOW-57-4	Tonga Trench, −20.25°S, 173.42°W	Harzburgite	Fresh	Oliv, Opx, Cpx
BMRG08-98-2-1	Tonga Trench, −19.25°S, 172.94°W	Harzburgite	Fresh	Oliv, Opx
NOVA-88-A1	Tonga Trench, −20.38°S, 173.27°W	Harzburgite	Fresh	Opx
		Xenoliths		
LS-33	Pali Aike volcanic field, Patagonia	Gt Lherz	Fresh	Oliv, Opx, Cpx
TMO	Pali Aike volcanic field, Patagonia	Gt-Sp Lherz	Fresh	Oliv, Opx, Cpx
SAV-AS1	Sverrejfell Volcano, Spitsbergen	Lherzolite	Fresh	Oliv, Opx, Cpx
SAV-AS2	Sverrejfell Volcano, Spitsbergen	Lherzolite	Fresh	Oliv, Opx, Cpx
SA-3-9	Savai'i Island, Samoa	Harzburgite	Fresh	Oliv, Opx
SAV-1-28	Savai'i Island, Samoa	Harzburgite	Fresh	Opx
		Orogenic Peridotite		
3923J01	Josephine Peridotite, Oregon	Harzburgite	Moderate	Oliv, Opx
3924J08	Josephine Peridotite, Oregon	Harzburgite	Moderate	Oliv, Opx
3925G01	Josephine Peridotite, Oregon	Harzburgite	Moderate	Oliv, Opx
JP08PS01	Josephine Peridotite, Oregon	Harzburgite	Moderate	Oliv, Opx, Cpx

of each grain. On each of the three mounts prepared, a piece of synthetic forsterite was included for use in monitoring background water concentrations [*Koga et al*., 2003]. Once all grains were mounted, the samples were polished using diamond suspensions down to 1 μm. The mounts were cleaned in ethanol and placed in a vacuum oven at 50°C for at least 12 h. Samples were removed from the vacuum oven and coated with gold immediately prior to analytical sessions.

Samples were analyzed using the Cameca 6f SIMS at the Department of Terrestrial Magnetism, Carnegie Institution of Washington [*Hauri et al*., 2002; *Koga et al*., 2003]. Analysis of water in NAMs requires minimal amounts of background volatiles, as monitored by the vacuum pressure in the sample chamber, which should be $<10^{-9}$ Torr. To achieve this, the SIMS underwent a 24 h bake-out prior to each analytical session. The machine was calibrated using a primary set of glass standards, followed by a secondary set of NAM-specific standards to create working curves for olivine, orthopyroxene, and clinopyroxene. To further maintain the ultrahigh vacuum, sample mounts were introduced into the exchange chamber at least 12 h prior to insertion into the main sample chamber. Sample mounts were left in the main sample chamber for an additional 12 h prior to data collection. In general, increases in background H_2O concentrations correlate with increases in sample chamber pressure.

Analyses were made using a rastered Cs^+ beam with a current of 15–20 nA. The sputter crater was 30–40 μm, but the smallest field aperture was used to limit ion collection to the central 10 μm diameter area. Using the electron multiplier, the masses ^{12}C, $^{16}O^1H$, ^{19}F, ^{30}Si, ^{31}P, ^{32}S, and ^{35}Cl were cycled through to collect five blocks of data. Intensities of $^{12}C/^{30}Si$, $^{32}S/^{30}Si$, and $^{35}Cl/^{30}Si$ were used to monitor for contamination. While grains were checked for optical purity using a petrographic microscope prior to analysis, values of these ratios

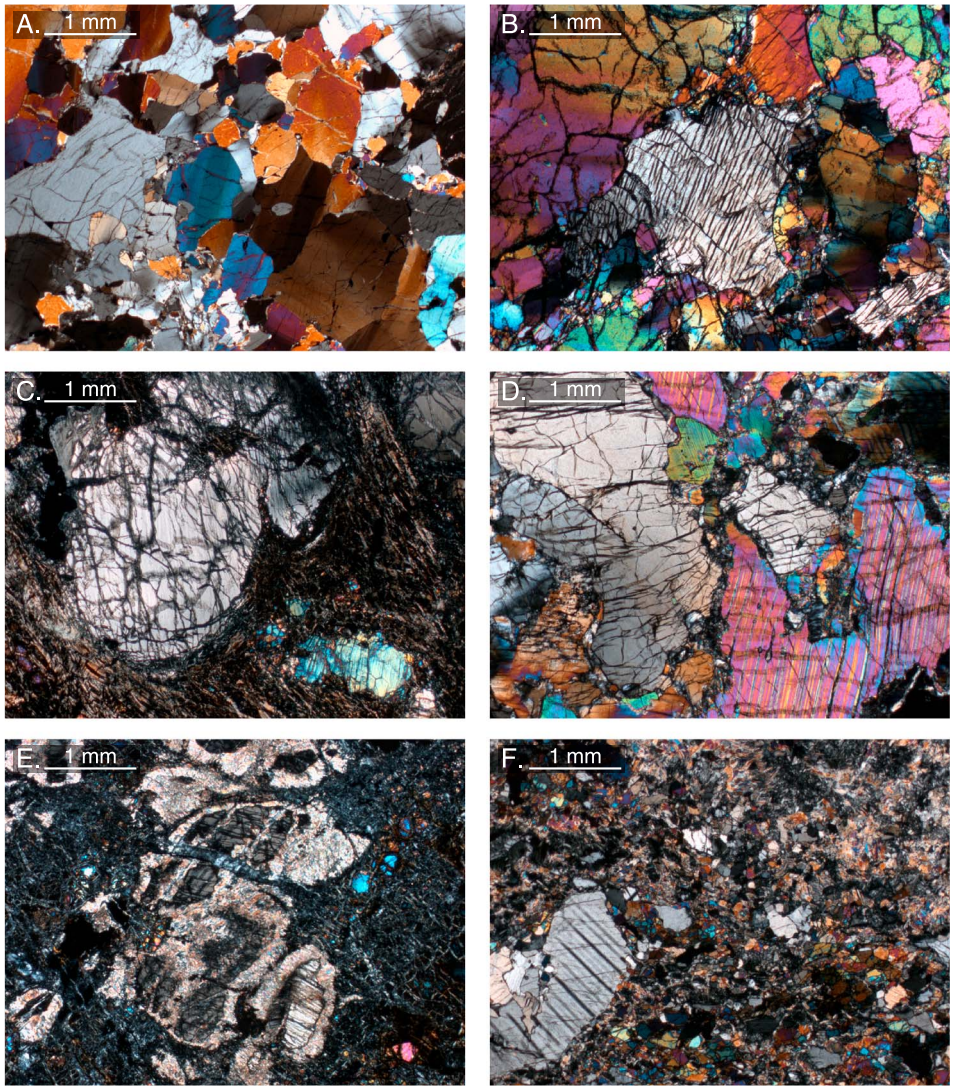

Figure 1. Photomicrographs of fresh and altered abyssal peridotites under cross-polarized light. (a) Tonga harzburgite BMRG08-98-2-1, fresh; (b) Gakkel harzburgite HLY0102-40-81, also fresh; (c) SWIR peridotite Van7-96-35, moderately altered; (d) SWIR pyroxenite vein Van7-96-09, low degree of alteration; (e) SWIR peridotite Van7-85-30, highly altered, with alteration coronas of amphibole around Opx; (f) SWIR pyroxenite vein Van7-96-16, highly altered, with fine-grained tremolite groundmass replacing pyroxene.

above background were taken as indicators of inclusions, fractures, or foreign material and were excluded from the data set. In addition, only analyses with steady count rates, as indicated by low standard deviations in $^{16}O^{1}H$ /^{30}Si, $^{19}F/^{30}Si$, and $^{31}P/^{30}Si$, were included in the data set (Table 2). Analysis of P was only included in the third analytical session.

Water concentrations were calculated by establishing working curves for olivine, Opx, and Cpx using standards calibrated by *Koga et al.* [2003] and *Aubaud et al.* [2007]. Standards used for olivine were KLV-23, GRR1012, ROM177, ROM250-2, and ROM250-13; for Opx A288, Enstatite-India, KBH-1, and ROM273-OG2; and for Cpx CM68, PMR-53, ROM273-10, ROM273-16, and ROM273-21. F and P concentrations were determined using basalt glass working curves [*Hauri et al.*, 2002], as no NAM-specific standards are available for these elements. Standards used were 519-4-1, 1654-3, 1833-1, 1833-11, 1846-12, D30-1, and WOK28-3.

The water concentration of the olivine standards is uncertain due to recent revisions in the FTIR calibration upon which some of the standards are based [*Kovács et al.*, 2010; *Withers et al.*, 2012] and due to heterogeneity in at least one of the olivine standards (KLV-23). However, previous studies have demonstrated

Table 2. Water Concentrations in Peridotite Minerals[a]

						H_2O		H/Si		F[b]		P[c]	
Sample	Type	Location	Lithology	Grains	Pts	ppm	±	ppm	±	ppm	±	ppm	±
					Olivine								
HLY0102-40-81	Abyssal	Gakkel	Harzburgite	1	7	2	2	35	34	0.04	0.02		
7TOW-57-4	Abyssal	Tonga Trench	Harzburgite	2	4	2.7	0.6	43	10	<0.01			
BMRG08-98-2-1	Abyssal	Tonga Trench	Harzburgite	2	12	3	1	53	17	<0.01			
LS-33	Xenolith	Pali Aike	Gt Lherz	2	11	13	5	220	82	1.3	0.2	39	2
TMO	Xenolith	Pali Aike	Gt-Sp Lherz	2	8	9	3	155	49	2.28	0.07	57	1
SAV-AS1	Xenolith	Spitsbergen	Lherzolite	2	7	4.2	0.6	68	10	0.20	0.02		
SAV-AS2	Xenolith	Spitsbergen	Lherzolite	2	4	6	1	100	17	0.02	0.01		
SA-3-9	Xenolith	Samoa	Harzburgite	1	2	4.1	0.5	67	9	0.10	0.04		
3923J01	Orogenic	Josephine	Harzburgite	2	4	9	3	154	54	<0.01			
3924J08	Orogenic	Josephine	Harzburgite	2	4	6.9	0.7	112	11	<0.01			
3925G01	Orogenic	Josephine	Harzburgite	1	2	8.4	0.5	137	9	<0.01			
JP08PS01	Orogenic	Josephine	Harzburgite	3	4	9	2	144	26	<0.01			
					Orthopyroxene								
PS86-6-38	Abyssal	SWIR	Lherzolite	2	4	171	22	1971	252	3.4	0.2		
Van7-85-30	Abyssal	SWIR	Harzburgite	2	4	*289*	*23*	*3327*	*263*	*0.15*	*0.04*		
Van7-85-42	Abyssal	SWIR	Lherzolite	2	3	145	8	1672	91	0.14	0.04		
Van7-85-47	Abyssal	SWIR	Lherzolite	2	5	157	16	1804	184	0.26	0.03		
Van7-85-49	Abyssal	SWIR	Lherzolite	1	2	198	12	2282	135	0.65	0.00		
Van7-96-09V	Abyssal	SWIR	Pyroxenite Vein	4	10	9	4	105	48	5	1	1.3	0.5
Van7-96-16V	Abyssal	SWIR	Pyroxenite Vein	4	8	*378*	*128*	*4348*	*1467*	*3*	*3*	*8*	*6*
Van7-96-18M	Abyssal	SWIR	Perid w/ Pyx Vn	2	5	36	48	411	546	9	1	15	4
Van7-96-18V	Abyssal	SWIR	Pyx Vn in Perid	1	4	22	5	251	52	8	2	2.6	0.2
Van7-96-21M	Abyssal	SWIR	Harz w/ Pyx Vn	4	6	147	10	1685	116	15	6	10	2
Van7-96-21V	Abyssal	SWIR	Pyx Vn in Harz	1	3	162	12	1860	140	12.6	0.9	12	1
Van7-96-25	Abyssal	SWIR	Lherzolite	2	2	21	13	237	144	5	1		
Van7-96-28	Abyssal	SWIR	Lherzolite	4	7	122	19	1404	221	10	4	5.6	0.4
Van7-96-35	Abyssal	SWIR	Lherzolite	1	1	87	8	998	88	12.6	0.2		
Van7-96-38	Abyssal	SWIR	Lherzolite	5	9	116	27	1337	306	2	1	15	1
HLY0102-40-81	Abyssal	Gakkel	Harzburgite	1	4	99	10	1133	117	1.4	0.1		
PS59-235-17	Abyssal	Gakkel	Lherzolite	3	13	145	18	1664	209	3.1	0.8		
7TOW-57-4	Abyssal	Tonga Trench	Harzburgite	1	6	91	8	1043	96	<0.1			
BMRG08-98-2-1	Abyssal	Tonga Trench	Harzburgite	2	4	77	10	885	120	<0.1			
NOVA-88-A1	Abyssal	Tonga Trench	Harzburgite	1	2	116	13	1335	154	<0.1			
LS-33	Xenolith	Pali Aike	Gt Lherz	2	6	216	18	2488	213	25.9	0.6	4.3	0.5
TMO	Xenolith	Pali Aike	Gt-Sp Lherz	2	6	287	9	3304	103	16.0	0.6	9	2
SAV-AS1	Xenolith	Spitsbergen	Lherzolite	2	7	186	5	2133	53	4.21	0.07		
SAV-AS2	Xenolith	Spitsbergen	Lherzolite	2	3	137	10	1576	119	1.9	0.1		
SA-3-9	Xenolith	Samoa	Harzburgite	1	2	99	9	1136	104	10.8	0.3		
SAV-1-28	Xenolith	Samoa	Harzburgite	1	3	118	11	1355	126	17.2	0.8		
3923J01	Orogenic	Josephine	Harzburgite	1	1	168	15	1934	168	<0.1			
3924J08	Orogenic	Josephine	Harzburgite	2	5	216	19	2487	220	<0.1			
3925G01	Orogenic	Josephine	Harzburgite	1	1	306	27	3516	305	<0.1			
JP08PS01	Orogenic	Josephine	Harzburgite	3	6	265	38	3048	440	<0.1			
					Clinopyroxene								
PS86-6-38	Abyssal	SWIR	Lherzolite	1	2	459	10	5594	118	10.3	0.3		
Van7-85-30	Abyssal	SWIR	Harzburgite	1	1	*793*	*69*	*9676*	*839*	*0.5*	*0.1*		
Van7-85-42	Abyssal	SWIR	Lherzolite	1	2	429	38	5229	463	0.7	0.1		
Van7-85-47	Abyssal	SWIR	Lherzolite	2	2	415	16	5059	197	1.3	0.4		
Van7-85-49	Abyssal	SWIR	Lherzolite	2	4	398	72	4855	881	3.1	0.2		
Van7-86-27	Abyssal	SWIR	Lherzolite	1	1	*748*	*65*	*9124*	*792*	*0.1*	*0.0*	*1.1*	*0.2*
Van7-96-09V	Abyssal	SWIR	Pyroxenite Vein	6	14	59	19	716	237	18.5	2.5	5.2	3.5
Van7-96-16V	Abyssal	SWIR	Pyroxenite Vein	1	1	*644*	*135*	*7856*	*1643*	*4.1*	*2.8*	*14.8*	*7.5*
Van7-96-18V	Abyssal	SWIR	Pyx Vn in Perid	1	2	550	7	6707	82	23.6	0.9	6.6	0.6
Van7-96-21M	Abyssal	SWIR	Harz w/ Pyx Vn	2	5	484	40	5908	494	43.9	8.4	25.5	1.2
Van7-96-21V	Abyssal	SWIR	Pyx Vn in Harz	3	5	401	283	4891	3446	34.1	30.3	28.7	3.8
Van7-96-25	Abyssal	SWIR	Lherzolite	2	4	458	33	5591	397	18.5	4.3	14.2	0.6

Table 2. (continued)

						H_2O		H/Si		F[b]		P[c]	
Sample	Type	Location	Lithology	Grains	Pts	ppm	±	ppm	±	ppm	±	ppm	±
Van7-96-28	Abyssal	SWIR	Lherzolite	3	6	613	35	7471	431	28.1	7.0	14.7	1.5
Van7-96-35	Abyssal	SWIR	Lherzolite	4	8	413	38	5038	458	66.2	9.7	7.2	0.9
Van7-96-38	Abyssal	SWIR	Lherzolite	1	1	665	58	8106	703	3.3	0.1		
PS59-235-17	Abyssal	Gakkel	Lherzolite	1	5	362	9	4418	115	10.1	2.4		
7TOW-57-4	Abyssal	Tonga Trench	Harzburgite	1	2	254	28	3094	345	0.3	0.1		
LS-33	Xenolith	Pali Aike	Gt Lherz	2	8	458	63	5587	772	52.9	0.6	18.6	0.4
TMO	Xenolith	Pali Aike	Gt-Sp Lherz	2	13	667	70	8132	853	47.4	2.7	32.0	2.2
SAV-AS1	Xenolith	Spitsbergen	Lherzolite	2	4	350	10	4270	119	13.3	1.0		
SAV-AS2	Xenolith	Spitsbergen	Lherzolite	2	4	301	77	3674	944	6.9	0.2		
JP08PS01	Orogenic	Josephine	Harzburgite	1	1	489	42	5960	517	<0.1			

[a]Results are reported as the average and standard deviation of all points analyzed for each mineral phase in a sample. Numbers in italics are samples that are moderately to highly altered.
[b]Detection limit for F is 0.01 ppm in olivine and 0.1 ppm in Opx and Cpx.
[c]Empty values correspond to grains for which P was not measured, as P was only analyzed in the final analytical session.

that SIMS working curves for olivine and Opx are identical within analytical uncertainty, suggesting similar matrix effects [*Koga et al*., 2003; *Kovács et al*., 2010; *Withers et al*., 2011; *Mosenfelder and Rossman*, 2013a]. We also observed similar working curves for Opx and olivine, and therefore used the Opx working curve to determine olivine water concentrations. Ultimately, uncertainties with respect to the olivine calibration are unimportant—in this study—as olivine does not preserve mantle water concentrations (discussed below).

Analyses were corrected for background concentrations of H_2O, F, and P by subtracting the concentrations measured in a synthetic forsterite crystal, SynFo68, which contains 40 ppb H_2O (determined by FTIR) [*Koga et al*., 2003]. The measured water concentration in SynFo68 provides an indication of the background water level in the mass spectrometer, which varied by session and sample mount. Each block of 10 sample analyses was bracketed by an analysis of SynFo68. Background water was 7.2 ± 0.7 ppm ($n = 7$) for the first sample mount, from 8.4 ± 0.3 ppm ($n = 15$) to 14 ± 2 ppm ($n = 2$) for the second mount, and from 15 ± 3 ppm ($n = 15$) to 20 ± 2 ppm ($n = 5$) for the third mount. Background corrections for F and P were applied assuming that SynFo68 contains none of these elements. Across three analytical sessions, background concentrations of F were 0.23 ± 0.02 ppm ($n = 7$), 0.21 ± 0.01 ppm ($n = 15$), and 0.085 ± 0.007 ppm ($n = 15$). The background concentration of P, which was only collected in the third session, was 1.01 ± 0.03 ppm ($n = 15$). All data reported in Tables 2 and S1–S3 in the supporting information have been background corrected.

Analytical error for individual volatile analyses (Tables S1–S3) was determined in various ways, including (i) variations in background water concentrations, (ii) analytical reproducibility, and (iii) count statistics. The error in background water concentration is given by the standard deviation in SynFo68 concentrations for a given group of analyses. Reproducibility for water concentrations was determined from eight repeat analyses of a homogeneous olivine grain from sample BMRG08-98-2-1, which gave a value of 3.8 ± 0.3 ppm (2σ), equivalent to 9% reproducibility. For H_2O, the precision indicated by the count statistics is generally better than the analytical reproducibility. An estimate of analytical reproducibility for F and P is provided by repeat analyses of grains from Pali Aike xenolith TMO. For olivine, five repeat analyses of a grain gave 1% reproducibility for F and 3% reproducibility for P. For Opx, three repeat analyses gave 1% reproducibility for F but 10% reproducibility for P. For Cpx, nine repeat analyses gave 7% reproducibility for both F and P. The standard deviation of background concentrations as measured in SynFo68 is 7%–15% for F and 3% for P. Due to the low concentrations of F and P in peridotite minerals, the count statistic error is sometimes greater than the reproducibility.

For individual analyses (Tables S1–S3), the reported analytical error is the error propagated by combining background error and analytical reproducibility. For the averages of all analyses per sample (Table 2), the reported error is the standard deviation of the average, which is always greater than the analytical error associated with individual analyses. If only one good analysis is available for a sample, the analytical error is used.

Trace element data were collected for a subset of clinopyroxenes in this study using the Cameca 6f SIMS. An O^- beam with 8–12 nA current and ~75 μm diameter was used with an accelerating voltage of 10 kV and an energy filter offset of −135 V. Working curves were determined using Cpx standards from *Eggins et al*.

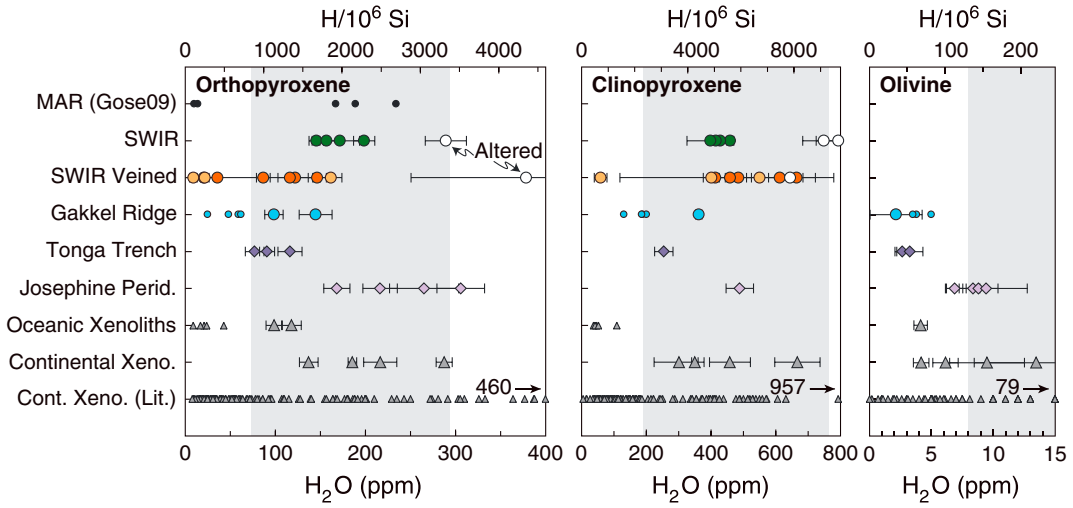

Figure 2. Ranges in water concentrations in peridotite NAMs. Larger symbols represent samples from this study and smaller symbols correspond to literature data. Error bars are 2σ standard deviations in the average of multiple analyses per sample. Three highly altered samples (see photomicrographs in Figure 1) are shown as white symbols. "SWIR Veined" refers to dredge Van7-96, which consists of pyroxenite veins (light orange) and host peridotites (dark orange). Grey shaded fields indicate the estimated water concentration ranges of upper mantle minerals, calculated from bulk upper mantle water (50–200 ppm) [*Hirschmann*, 2006], mineral modes [*Workman and Hart*, 2005], and mineral/mineral partition coefficients (see Table 3 for details). Literature data: Mid-Atlantic Ridge (MAR) abyssal peridotites from *Gose et al.* [2009] and *Schmädicke et al.* [2011]; additional Gakkel peridotites from *Peslier* [2010]; xenoliths from *Bell and Rossman* [1992], *Peslier et al.* [2002], *Demouchy et al.* [2006], *Peslier and Luhr* [2006], *Aubaud et al.* [2007], *Grant et al.* [2007b], *Falus et al.* [2008], *Li et al.* [2008], *Yang et al.* [2008], *Bonadiman et al.* [2009], and *Xia et al.* [2010]. Note that while xenoliths appear to extend to 0 ppm H_2O, the lowest concentration is 8 ppm in Opx, 5 ppm in Cpx, and 0.2 ppm in olivine.

[1998] and *Norman* [1998]. The calibration was checked against KH1 Cpx [*Irving and Frey*, 1984], for which the measured values of trace elements were found to be within 25% of the accepted values (typical for low-concentration trace elements). Concentrations of Gd, Dy, Er, Yb, and Hf were corrected for oxide interferences, as discussed by *Hellebrand et al.* [2002].

Major element data (Table S4) were not collected in this study, as they were already available for the SWIR [*Warren et al.*, 2009], Gakkel Ridge (H. J. B. Dick, personal communication, 2007), Josephine Peridotite [*Skemer et al.*, 2010], Samoa xenoliths [*Hauri and Hart*, 1994], and Pali Aike xenoliths [*Stern et al.*, 1989].

4. Results

Results from the analysis of H_2O, F, and P in olivine, Opx, and Cpx from 31 peridotites are given in Table 2. Results are averaged by sample, with data for individual analyses given in Tables S1–S3. Water concentrations in olivine vary from 0.4 to 22 ppm, in Opx from 2 to 521 ppm, and in Cpx from 42 to 735 ppm (Figure 2). Concentrations of F range from 0.02 to 2 ppm in olivine, 0.1 to 26 ppm in Opx, and 0.1 to 66 ppm in Cpx (Figure 3). Several samples were below detection limit for F (Table 1), which is estimated as 0.01 ppm for olivine and 0.1 ppm for pyroxenes. The concentration of P in olivine was only measured in the Pali Aike samples, which have an average concentration of 48 ppm. For pyroxenes, P—which was only measured in Pali Aike and SWIR pyroxenite-veined peridotites—ranged from 1 to 15 ppm in Opx and 5 to 32 ppm in Cpx (Figure 3).

Water concentrations measured in this study are within the range of previous measurements of olivine and pyroxenes from peridotite xenoliths [e.g., *Peslier*, 2010], as shown in Figure 2. Data also plot within the range for model upper mantle mineral concentrations (Table 3), calculated from the estimated range of water in the bulk upper mantle [*Hirschmann*, 2006]. However, as discussed below, olivine concentrations are relatively low and appear to have diffusively lost water, whereas pyroxenes provide a robust means of constraining upper mantle water variations.

Two Pali Aike xenoliths were analyzed in order to provide a comparison to previous FTIR data from this locality. *Demouchy et al.* [2006] measured 28 ± 10 and 32 ± 10 ppm H_2O in two olivine grains from xenolith

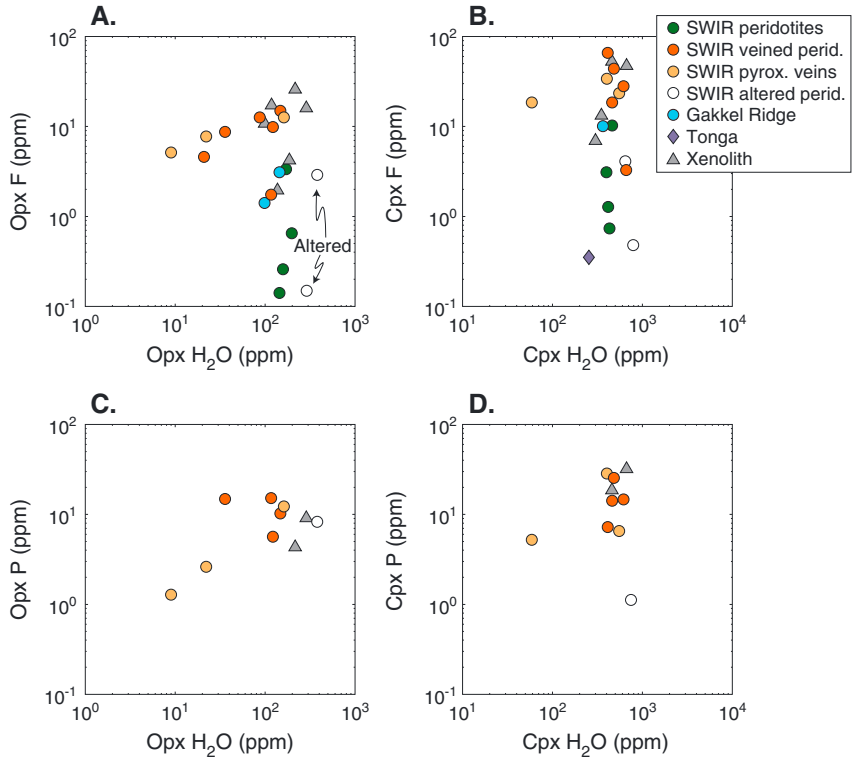

Figure 3. Variations in pyroxene F and P concentrations as a function of water concentrations. The fewer number of data points in C and D reflects the fact that P was only measured during the final analytical session.

LS33. For comparison, the two LS33 olivines in this study have 12 ± 3 and 15 ± 6 ppm H_2O (Tables S1–S3). These results are in reasonable agreement given that *Demouchy et al*. [2006] determined that Pali Aike olivines have undergone variable degrees of diffusive water loss during ascent. Pyroxene data are unfortunately not available for the exact same xenoliths. In Pali Aike xenolith Palix-1, which was measured by FTIR by *Demouchy et al*. [2006], Opx = 310 ± 105 ppm and Cpx = 416 ± 150 ppm. For comparison, SIMS analyses in this study give Opx = 216 ± 18 ppm, Cpx = 458 ± 63 ppm for LS33 and Opx = 287 ± 9 ppm, Cpx = 667 ± 70 ppm for TMO. These values are in reasonable agreement if some of the variability is assumed to reflect local variations in water content.

Peridotites from different tectonic environments show distinct ranges in water concentrations (Figure 2), although the sample set is small. Ridge peridotites extend to very low concentrations, especially when previously published data are included for the Gakkel Sparsely Magmatic Zone [*Peslier*, 2010] and the

Table 3. Mineral Water Concentrations in the Model Upper Mantle[a]

	Bulk		Olivine		Opx		Cpx	
Concentration (ppm)	H_2O	H/Si	H_2O	H/Si	H_2O	H/Si	H_2O	H/Si
Minimum estimate	50[b]	626	8	132	73	844	191	2329
Maximum estimate	200[b]	2505	32	527	294	3377	764	9316
Mineral mode[c]			57%		28%		13%	
Conversion factor[d]	13		16		11		12	

[a]Mineral water concentrations determined from the bulk upper mantle water concentration, assuming $D^{Ol/Opx} = 0.11$ (experimental average) and $D^{Cpx/Opx} = 2.6$ (xenolith average). See Figures 2 and 6 for references for these partition coefficient data sets. Spinel is assumed to contain negligible amounts of water.
[b]Upper mantle water estimate from *Hirschmann* [2006].
[c]Mineral modes for model upper mantle from *Workman and Hart* [2005].
[d]Conversion factor between ppm H_2O and ppm H/Si.

Fifteen-Twenty region on the Mid-Atlantic Ridge (MAR) [*Schmädicke et al*., 2011]. Veined peridotites from the SWIR Oblique Segment extend to very low concentrations and have the largest range in water concentrations for any individual location. Subduction zone samples (Tonga Trench and Josephine Peridotite) bracket almost the full range of concentrations, with the Josephine Peridotite having relatively high concentrations whereas Tonga is relatively depleted. Combined with published data, xenoliths have the largest range of concentrations, but they represent many tectonic environments. Oceanic xenoliths from Samoa (this study) and Cape Verde [*Bonadiman et al*., 2009] overlap the range of seafloor peridotites and have lower concentrations than continental xenoliths.

Pyroxene trace element data are provided in Table 4 and rare earth element (REE) plots are shown in Figure 4. The SWIR and Gakkel peridotites have typical, depleted patterns for abyssal peridotites, except for the SWIR pyroxenite-veined samples. Josephine and Tonga peridotites are extremely depleted, with some elements below the detection limit (~1 ppb). Xenoliths are variably enriched, reflecting the varied origin of these peridotites.

5. Discussion of Water in Peridotite NAMs

5.1. Effect of Alteration on NAMs

A major concern for the analysis of abyssal and orogenic peridotites is the potential effect of incipient serpentinization, followed by diffusive exchange of water between serpentine and NAMs. An additional concern is incipient hydration of NAMs at spatial scales not readily identifiable by optical microscopy. We assess the effect of alteration on measured water concentrations by (i) petrographic analysis; (ii) examining the data set for analyses that show high C, Cl, or S counts; (iii) diffusion modeling; and (iv) comparison of results between fresh and altered samples.

Samples in this study are a mixture of fresh (Tonga, Gakkel, xenoliths) and altered (SWIR, Josephine) peridotites. In general, xenoliths are the least altered and the SWIR abyssal peridotites are the most altered. Alteration mainly occurs as slight to moderate replacement of olivine by serpentine, brucite, and magnetite. In three SWIR samples (Van7-85-30, Van7-86-27, and Van7-96-16), pyroxenes are partly replaced by tremolite (Figure 1), which occurs at temperatures >350°C [*Bach et al*., 2004; *Bach and Klein*, 2009].

Very strict data filtering was applied to aid in the identification of alteration effects on NAM water concentrations. Of 424 data points collected, 120 analyses (28%) were discarded due to high C, Cl, or S counts or due to large standard deviations in OH, F, or P counts. Concentrations for rejected analyses range up to 470 ppm in olivine, 3000 ppm in Opx, and 16,000 ppm in Cpx. Analyses in which concentrations are only slightly elevated, but analytical indicators are high, probably reflect incipient alteration. Approximately 90% of rejected analyses are from SWIR and Josephine samples, which have the highest levels of alteration (Figure 1).

Analyses classified as mantle (i.e., pre-alteration) values are strongly dependent on mineral phase. Forty-five percent of Cpx analyses are excluded from the final data set, whereas only 20% of olivine and 16% of Opx analyses are excluded. Among SWIR samples, comparatively more Cpx was measured in an effort to obtain reliable H_2O concentration data, but only 59 of 129 analyses correspond to mantle water contents. In contrast, Opx produced consistently better data, with 73 of 96 SWIR analyses included in the final data set. Difficulties with Cpx analyses may reflect a higher rate of incipient alteration, possibly due to wider exsolution lamellae in Cpx in comparison to Opx. Thus, Opx in natural peridotites is the most important NAM for constraining upper mantle water concentrations.

Three of the abyssal peridotites are too altered to produce reliable data: Van7-85-30, Van7-86-27, and Van7-96-16. In these samples, few reliable data were obtained despite many analyses, and even these have relatively high water concentrations: 650–800 ppm H_2O in Cpx and 300–400 ppm in Opx (Figure 2). Petrographic observation indicates high degrees of alteration, including partial replacement of pyroxene by amphibole. For example, the photomicrograph of Van7-85-30 (Figure 1e) shows alteration haloes around Opx. Van7-96-16 consists of coarse grained, relatively unaltered regions that are crosscut by fine-grained zones where pyroxenes have been replaced by amphibole (Figure 1f).

Previous Sr isotopic analyses for two of the three highly altered peridotites confirm that they have undergone extensive exchange with seawater. For example, Cpx from Van7-85-30 and Van7-86-27 have $^{87}Sr/^{86}Sr > 0.704$ [*Warren et al*., 2009]. In comparison, the upper mantle has $^{87}Sr/^{86}Sr \approx 0.702$ and seawater has $^{87}Sr/^{86}Sr = 0.709$. All samples from *Warren et al*. [2009] were extensively leached to remove surficial alteration prior to Sr isotopic

Table 4. Trace Element Concentrations in Cpx and Opx

Sample	Type	Location	P	K	Sc	Ti	Cr	Sr	Y	Zr	Nb
					Clinopyroxene						
PS86-6-38	Abyssal	SWIR				2412	4581	6.28	18.90	8.67	0.002
Van7-85-30	Abyssal	SWIR				1291	6284	0.75	13.69	1.39	
Van7-85-42	Abyssal	SWIR				1220	5863	0.75	12.52	1.01	0.004
Van7-85-47	Abyssal	SWIR				1011	4947	0.38	12.23	0.45	0.004
Van7-85-49	Abyssal	SWIR				1001	5151	1.55	13.46	0.88	0.003
Van7-86-27	Abyssal	SWIR				879	4001	0.81	7.49	0.48	
Van7-96-09V	Abyssal	SWIR	32	11	54	2162	4208	10.13	19.89	15.04	0.087
Van7-96-16V	Abyssal	SWIR				4091	3150	4.01	33.01	38.65	
Van7-96-18M	Abyssal	SWIR				2952	4313	12.59	23.58	20.63	
Van7-96-18V	Abyssal	SWIR				2700	2811	3.41	26.05	18.90	
Van7-96-21M	Abyssal	SWIR				3356	4484	24.40	18.77	35.62	
Van7-96-21V	Abyssal	SWIR				4040	4495	21.65	20.47	45.74	
Van7-96-25	Abyssal	SWIR				2538	5574	10.96	16.43	17.17	
Van7-96-28	Abyssal	SWIR				2289	6529	76.14	11.31	18.08	
Van7-96-35	Abyssal	SWIR				1798	8083	34.67	12.51	21.73	
Van7-96-38	Abyssal	SWIR				2699	3948	11.81	20.04	15.25	0.003
PS59-235-17	Abyssal	Gakkel	11	3	45	1390	7182	2.18	12.73	2.29	0.137
7TOW-57-4	Abyssal	Tonga SZ	2	7	47	34	5158	0.54	0.32	0.12	0.143
NOVA-88-A1	Abyssal	Tonga SZ	1	4	48	59	5163	0.30	0.49	0.29	0.145
LS-33	Xenolith	Pali Aike	26	79	23	2147	8047	80.29	4.81	17.56	0.506
TMO	Xenolith	Pali Aike	34	19	27	3134	6247	76.70	4.64	25.73	0.716
SAV-AS1	Xenolith	Spitsbergen	52	3	64	2496	4426	288.74	16.83	34.57	0.099
SAV-AS2	Xenolith	Spitsbergen	35	4	63	2164	4337	53.22	15.67	7.81	0.088
SA-3-9	Xenolith	Samoa			32	27	6612	0.2		2.05	
SAV-1-28	Xenolith	Samoa			34	257	5903	158.8		27.43	
JP08PS01	Orogenic	Josephine	28	7	39	212	8579	0.44	1.37	0.10	0.128
					Orthopyroxene						
Van7-85-42	Abyssal	SWIR							1.87		0.003
Van7-85-47	Abyssal	SWIR							1.82	0.01	0.003
Van7-85-49	Abyssal	SWIR						0.02	1.86		
Van7-96-09V	Abyssal	SWIR	30	3	25	696	1662	0.36	2.46	2.09	0.004
Van7-96-21M	Abyssal	SWIR						0.72	2.35	4.28	0.001
Van7-96-25	Abyssal	SWIR	54	4	16	601	3606	0.37	1.07	1.15	0.009
Van7-96-28	Abyssal	SWIR						1.65	1.41	1.65	0.013
Van7-96-38	Abyssal	SWIR						0.23	2.57	2.01	
SAV-1-28	Xenolith	Samoa				7.4		0.22		2.2	

[a]Data in this study collected by 6f SIMS at DTM; *Warren* [2007] collected by solution ICPMS at ISEI, Misasa and 3f SIMS at NENIMF, WHOI; *Warren et al.* [2009] collected by solution ICPMS at ISEI, Misasa; *Hauri et al.* [1993] and *Hauri and Hart* [1994] collected by 3f SIMS at NENIMF, WHOI.

analysis. Only Van7-85-30 and Van7-86-27 produced high $^{87}Sr/^{86}Sr$, whereas other samples from dredge Van7-85 have $^{87}Sr/^{86}Sr \approx 0.702$. *Warren et al.* [2009] interpreted the elevated $^{87}Sr/^{86}Sr$ ratios in Van7-85-30 and Van7-86-27 to reflect extensive reaction with seawater, resulting in partial replacement of pyroxene by tremolite. Based on these observations, the three highly altered peridotites are excluded from further discussion and analysis.

The high water concentration of pyroxenes in highly altered peridotites indicates that water can be added to NAMs at high levels of alteration. Alteration could also remove water from NAMs, as found in a study by *Andrut et al.* [2003] of metamorphic diopside, in which dissolved water decreased in the vicinity of amphibole lamellae. However, we did not find any evidence that alteration decreases water concentrations, based on the absence of pyroxene zonation and the high water contents in the most altered samples.

Even when alteration is not extensive (i.e., low water/rock ratios), diffusive exchange between serpentine and NAMs could potentially influence olivine and pyroxene water concentrations. Serpentinization typically occurs over the range 50–250°C [*Alt et al.*, 2007] and is generally insignificant above ~330°C [*Klein et al.*, 2009]. At 300°C, the hydrogen diffusion coefficient in olivine is $\sim 10^{-26}$ m^2/s [*Kohlstedt and Mackwell*, 1998; *Demouchy et al.*, 2006], which corresponds to a diffusion distance of only a few microns over tens of millions of years. Similarly, *Gose et al.* [2011] concluded that, below 300°C, hydrogen diffusion is too slow in Opx for

Table 4. (continued)

Ba	La	Ce	Nd	Sm	Eu	Gd	Dy	Er	Yb	Hf	Data Source[a]
						Clinopyroxene					
	0.037	0.569	2.385	1.338	0.587	2.170	2.843	1.584	1.524	0.456	*Warren* [2007]
	0.030	0.030	0.287	0.397	0.213	0.999	1.681	1.059	1.014		*Warren* [2007]
	0.016	0.023	0.257	0.401	0.203	0.994	1.708	1.128	1.077	0.096	*Warren* [2007]
	0.007	0.015	0.270	0.385	0.185	1.010	1.729	1.141	1.077	0.086	*Warren* [2007]
	0.013	0.025	0.283	0.427	0.211	1.189	1.838	1.161	1.150	0.079	*Warren* [2007]
0.218	0.005	0.013	0.144	0.305	0.142	0.707	1.371	0.860	0.859		*Warren* [2007]
0.028	0.258	1.562	3.235	1.379	0.562	2.204	3.165	2.133	2.079	0.795	This study
0.101	0.072	1.095	3.490	1.848	0.603	2.117	3.850	2.448	2.138		*Warren* [2007]
	0.227	1.870	2.829	1.412	0.595		2.817	1.750	1.597		*Warren* [2007]
	0.150	1.492	2.757	1.517	0.562		3.816	2.490	2.312		*Warren* [2007]
	0.976	5.133	6.087	2.084	0.800	2.372	2.857	1.729	1.518		*Warren* [2007]
	1.037	5.277	6.205	2.245	0.779	2.366	2.996	1.729	1.623		*Warren* [2007]
	0.171	1.444	2.429	1.154	0.513	1.863	2.342	1.407	1.343		*Warren* [2007]
	1.070	4.005	3.517	1.248	0.485	1.575	1.687	0.916	0.927		*Warren* [2007]
	0.399	2.209	3.143	1.402	0.538	1.824	2.025	1.028	0.996		*Warren* [2007]
	0.079	0.956	2.699	1.440	0.637	2.176	2.992	1.909	1.694	0.642	*Warren* [2007]
0.021	0.067	0.241	0.897	0.694	0.313	1.302	1.953	1.341	1.256	0.377	This study
0.017	0.012	0.017	0.007	0.002	0.002	0.008	0.017	0.056	0.141	0.003	This study
0.027	0.029	0.068	0.024	0.010	0.001	0.009	0.034	0.080	0.181	0.009	This study
0.101	1.251	4.536	4.391	1.301	0.416	1.239	1.034	0.424	0.315	0.669	This study
0.022	1.708	4.519	4.527	1.475	0.440	1.426	1.123	0.373	0.240	0.865	This study
0.092	15.402	22.428	6.557	1.599	0.603	2.192	2.813	1.848	1.750	1.236	This study
0.041	4.981	7.383	2.930	0.998	0.419	1.770	2.525	1.726	1.589	0.652	This study
	0.29	0.20	0.03	0.01	0.01		0.03	0.07	0.13		*Hauri and Hart* [1994]
	42.97	111.57	49.20	9.21	2.20		3.62		1.44		*Hauri et al.* [1993]
0.044	0.014	0.012	0.002			0.059	0.131	0.129	0.246	0.014	This study
						Orthopyroxene					
	0.002		0.007	0.016	0.011	0.066	0.220	0.218	0.341	0.010	*Warren et al.* [2009]
			0.007	0.011	0.010	0.063	0.200	0.220	0.341	0.018	*Warren et al.* [2009]
				0.016	0.010	0.066	0.209	0.211	0.336	0.011	*Warren et al.* [2009]
0.028	0.014	0.019	0.057	0.041	0.012	0.099	0.285	0.325	0.491	0.107	This study
	0.019	0.102	0.169	0.087	0.038	0.162	0.309	0.271	0.389	0.156	*Warren et al.* [2009]
0.023	0.048	0.021	0.032	0.020	0.006	0.051	0.126	0.135	0.234	0.051	This study
	0.020	0.057	0.085	0.054	0.022	0.096	0.183	0.152	0.225	0.061	*Warren et al.* [2009]
		0.018	0.067	0.054	0.026	0.128	0.309	0.279	0.408	0.115	*Warren et al.* [2009]
	0.13	0.19	0.33	0.09	0.04		0.23	0.18	0.28		*Hauri et al.* [1993]

serpentinization to change water concentrations in millimeter-sized crystals. In addition, they used IR mapping to show that defect water is relatively homogeneously distributed in Opx from MAR peridotites and is unrelated to the presence of serpentine in grain cracks. Thus, incipient serpentinization is not expected to increase water concentrations throughout peridotite minerals.

Comparison of altered peridotites to unaltered peridotites also suggests that low levels of alteration do not influence NAM water concentrations. For example, the two Gakkel peridotites—which are very fresh (Figure 1)—have Opx H_2O concentrations of ~100–150 ppm. Among the altered SWIR peridotites (excluding the three highly altered samples), unveined peridotites have ~150–200 ppm, while the peridotite matrix and pyroxenite veins in a set of veined peridotites have ~20–150 ppm. If the difference in water concentration is due to variable degrees of alteration—instead of variations related to tectonic setting—then the SWIR peridotites should have uniformly higher water concentrations, which they do not. Thus, we conclude that abyssal and orogenic peridotites can be analyzed for volatile concentrations, as long as they have low to moderate levels of alteration and analyses are not made in the vicinity of incipient serpentinization.

5.2. Diffusive Loss of Water During Peridotite Emplacement

A second major concern when analyzing peridotite NAMs is that the minerals have diffusively lost water during emplacement. Xenolith studies have often found that water in olivine is diffusively lost during emplacement [e.g., *Demouchy et al.*, 2006; *Peslier and Luhr*, 2006; *Li et al.*, 2008; *Denis et al.*, 2013]. In this study,

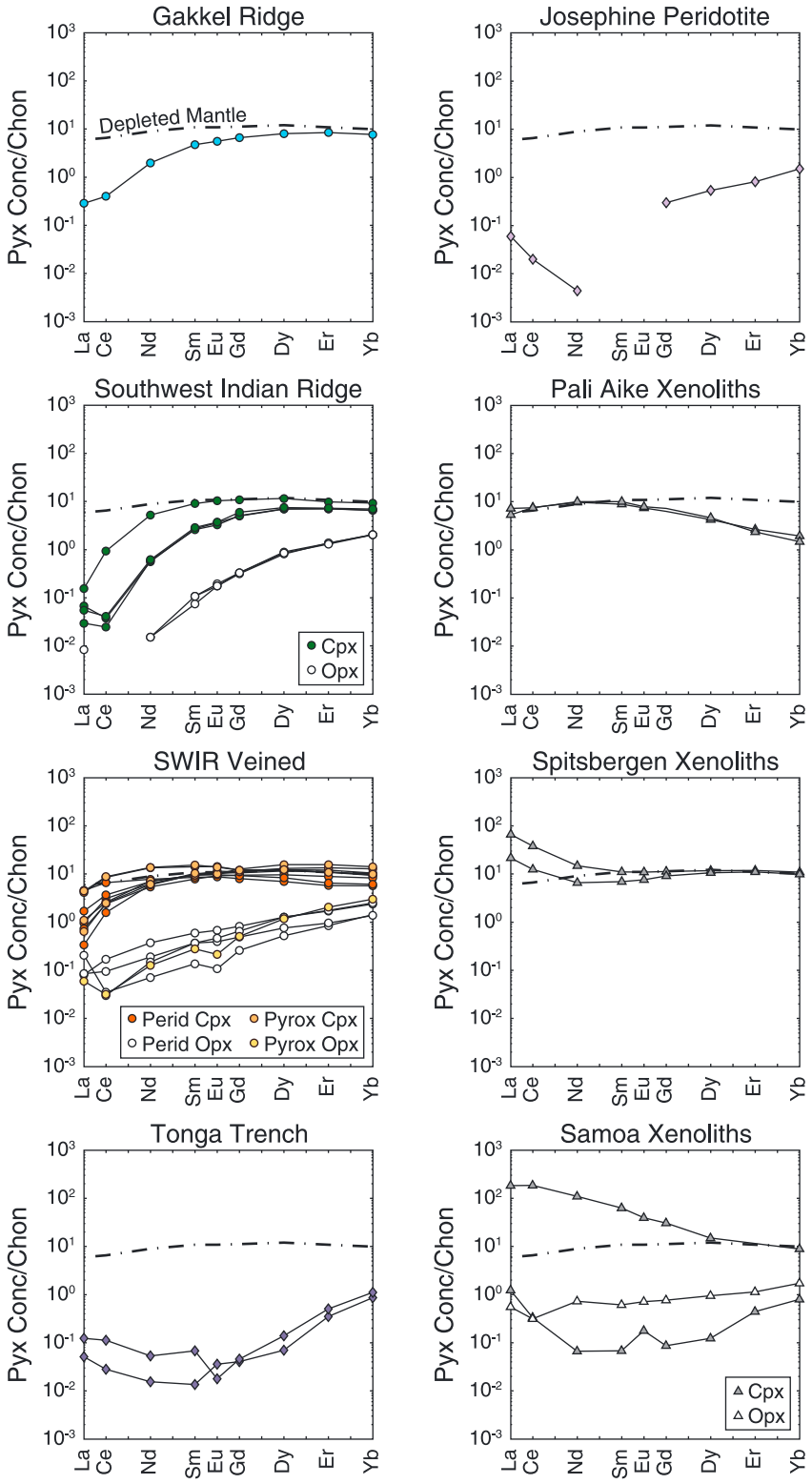

Figure 4. Plots of REE variations in peridotite Cpx and Opx; data are for Cpx unless noted in the legend. Data for SWIR samples are from *Warren* [2007] and *Warren et al*. [2009]; data for Pali Aike xenoliths are from *Hauri et al*. [1993] and *Hauri and Hart* [1994]; all other data are from this study (Table 4). Concentrations are normalized to chondrite [*Anders and Grevesse*, 1989]. The dashed line is the reference value for Cpx in the upper mantle before melting begins (depleted mantle or DM) [*Workman and Hart*, 2005].

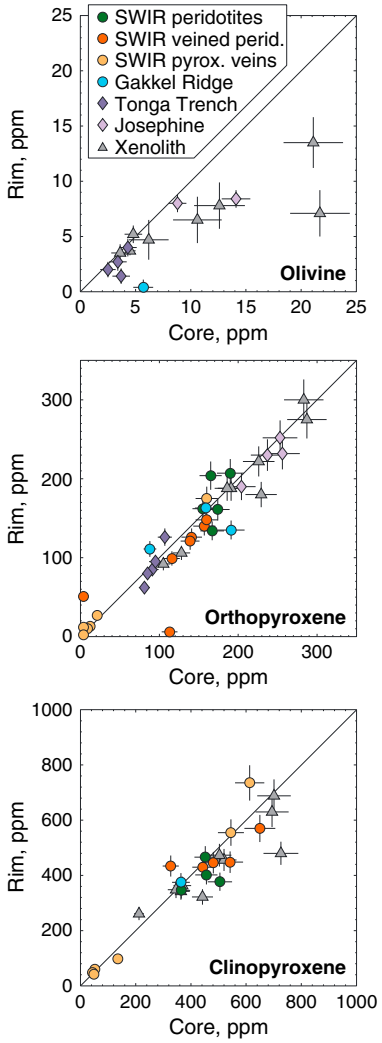

Figure 5. Paired core and rim water concentration analyses in individual grains. Most pyroxenes have similar core and rim concentrations, plotting within error of the 1:1 correlation line. Olivine shows significant disequilibrium, with rims having lower concentrations.

olivines also appear to have lost water, while pyroxenes have maintained their pre-emplacement compositions. This conclusion is based on three lines of evidence: (i) Water concentrations are >100 ppm in most pyroxenes, but are <15 ppm in olivines (Figure 2); (ii) zonation occurs in some olivines, but not in any pyroxene (Figure 5); and (iii) partitioning between Cpx and Opx suggests equilibrium, whereas partitioning between olivine and Cpx or Opx indicates disequilibrium (Figure 6).

Water zonation in olivine is shown in Figure 5 for grains with both core and rim analyses. Olivine plots significantly off the 1:1 correlation line, as many cores have higher concentrations than rims—most notably when cores have >10 ppm H_2O. Disequilibrium occurs between olivine cores and rims in all peridotite types (xenolith, orogenic, and abyssal). In addition, olivine water concentrations are <15 ppm for all samples. These two observations are interpreted as evidence for diffusive loss of water from olivine during peridotite emplacement.

Pyroxenes do not appear to have undergone diffusive water loss. In Figure 5, pyroxene cores and rims scatter around the 1:1 correlation line. In particular, Opx shows the best correspondence between cores and rims, with only two points plotting significantly off the line. Both of these points are from sample Van7-96-18M, which is the matrix of a pyroxenite-veined peridotite. The variability in this sample may reflect magmatic reaction between the host peridotite and lower concentration melts that produced pyroxene with low water contents.

Mineral-mineral partition coefficients ($D_{H_2O}^{Min/Min}$) also support the interpretation that olivine has lost water, but that pyroxenes have not (Table 5). In Figure 6, $D_{H_2O}^{Cpx/Opx}$ shows little variation and is similar in value to experimentally determined partition coefficients, suggesting that pyroxenes are in equilibrium. In contrast, $D_{H_2O}^{Ol/Opx}$ and $D_{H_2O}^{Ol/Cpx}$ cover a large range of values in natural samples, with many plotting at lower olivine water contents than predicted by experimental $D_{H_2O}^{Ol/Opx}$ and $D_{H_2O}^{Ol/Cpx}$. Similar observations have been made in other xenolith studies [e.g., *Xia et al.*, 2010; *Yu et al.*, 2011].

The low water concentration in a subset of the SWIR veined samples (Figure 2), which is most pronounced in pyroxenite sample Van7-96-09, could be interpreted as diffusive water loss. However, other samples in this dredge have concentrations up to 160 ppm in Opx and 650 ppm in Cpx. As all samples from a dredge have the same emplacement history, it is unlikely that they had different degassing histories. Additionally, the pyroxene grain size in Van7-96-09 is larger than any of the other samples (Figure 1d), meaning it is the least likely to record diffusive water loss. Hence, the low H_2O concentrations in Van7-96-09 are interpreted as having a high-temperature origin, with variations among samples in this dredge best explained by melt-peridotite interaction.

5.3. Comparison to Experimental Diffusion Data

As discussed above, natural pyroxenes in this study appear to have retained their mantle water contents, whereas olivines have lost water. Other xenolith studies have made similar observations [e.g., *Peslier et al.*,

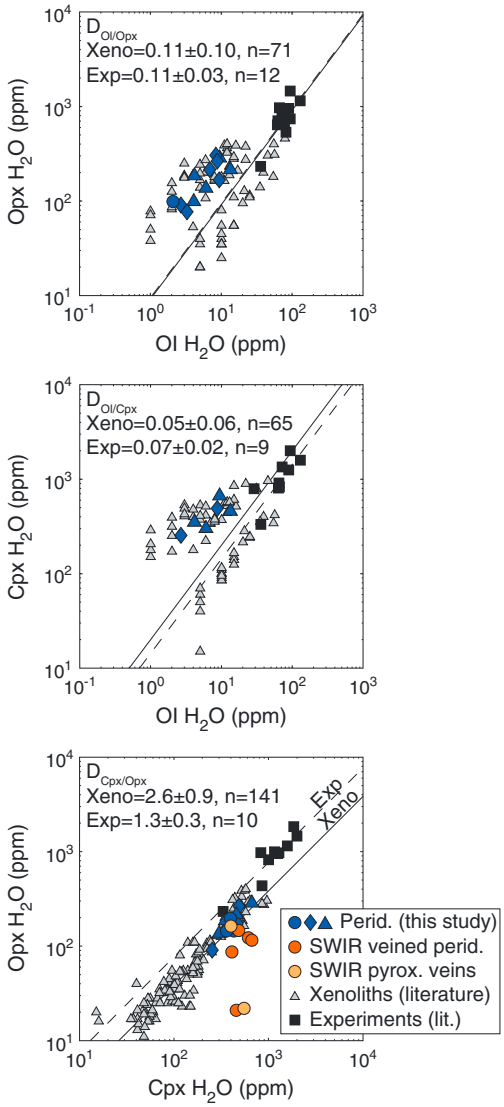

Figure 6. Covariations of olivine, Opx, and Cpx water concentrations, compared to literature data for xenoliths (see references in Figure 2) and experiments [*Aubaud et al.*, 2004, 2008; *Hauri et al.*, 2006; *Tenner et al.*, 2009; *O'Leary et al.*, 2010]. Circles indicate ridge peridotites, diamonds indicate subduction peridotites, and triangles indicate xenoliths. The lines represent regressions for $D_{H_2O}^{Ol/Opx}$, $D_{H_2O}^{Ol/Cpx}$, and $D_{H_2O}^{Cpx/Opx}$ based on alumina-bearing low-pressure experimental data (dashed lines) and xenolith data (solid lines). Average values for the xenolith partition coefficients do not include samples from this study.

2002, 2012; *Grant et al.*, 2007a; *Peslier*, 2010; *Xia et al.*, 2010; *Sundvall and Stalder*, 2011; *Yu et al.*, 2011]. Profiles across magmatic Cpx phenocrysts also indicate minimal water loss [*Wade et al.*, 2008; *Nazzareni et al.*, 2011; *Sundvall and Stalder*, 2011]. However, these observations are in disagreement with diffusion experiments for hydrogen, which have found $D_H \approx 10^{-9}$–10^{-12} m^2/s at 1000°C for both olivine and pyroxene [*Mackwell and Kohlstedt*, 1990; *Ingrin et al.*, 1995; *Kohlstedt and Mackwell*, 1998; *Hercule and Ingrin*, 1999; *Woods et al.*, 2000; *Stalder and Skogby*, 2003; *Demouchy and Mackwell*, 2006; *Ingrin and Blanchard*, 2006; *Farver*, 2010]. The symbol D_H is used here to refer to hydrogen diffusion coefficients, while $D_{H_2O}^{Ol/Opx}$, $D_{H_2O}^{Ol/Cpx}$, and $D_{H_2O}^{Cpx/Opx}$ refer to water partition coefficients. If hydrogen diffuses out of pyroxene at the same rate as olivine, then pyroxenes should not have such high water concentrations. For example, for $D_H = 10^{-12}$ m^2/s at 1000°C, pyroxene grains of 1 cm radius would reequilibrate in <3 years. In order for pyroxenes to retain water for >1 Myr, the effective diffusion coefficient at 1000°C needs to be $<10^{-18}$ m^2/s, or at least 6 orders of magnitude lower.

Possible explanations for the discrepancy between experimentally-determined diffusion rates and observations of natural pyroxenes fall into two categories: (i) differences between experimental conditions and mantle conditions [e.g., *Sundvall and Stalder*, 2011] and (ii) hydrogen loss that is rate limited by other mechanisms [e.g., *Grant et al.*, 2007a; *Sundvall and Skogby*, 2010; *Peslier et al.*, 2012]. In contrast to olivine, experimental diffusion data for pyroxene have only been collected at room pressure and often at reducing conditions relative to the upper mantle [*Ingrin et al.*, 1995; *Hercule and Ingrin*, 1999; *Woods et al.*, 2000; *Stalder and Skogby*, 2003; *Ingrin and Blanchard*, 2006]. The extent to which these diffusion coefficients are applicable at mantle conditions is thus unconstrained. However, making measurements at the correct conditions may not necessarily result in diffusion coefficients that are 6 (or more) orders of magnitude slower.

The second explanation for the discrepancy between diffusion experiments and natural pyroxenes is that H dehydration is rate limited by the movement of either electron holes or cations. *Hercule and Ingrin* [1999] suggested that the slower diffusion of H in pyroxene during incorporation/extraction experiments, in comparison to self-diffusion experiments, reflects H mobility controlled by electron hole counterflux. In this mechanism, the movement of electron holes depends on pyroxene Fe content, with increasing Fe content yielding increased electron hole mobility due to the exchange reaction: $Fe^{3+} + O^{2-} + 1/2H_2 \leftrightarrow Fe^{2+} + OH^-$.

Table 5. Water Partition Coefficients Derived From Mineral Data

Sample	Type	Location	Lithology	$D_{H_2O}^{Ol/Opx}$	$D_{H_2O}^{Ol/Opx}$	$D_{H_2O}^{Cpx/Opx}$
PS86-6-38	Abyssal	SWIR	Lherzolite			2.7
Van7-85-42	Abyssal	SWIR	Lherzolite			2.9
Van7-85-47	Abyssal	SWIR	Lherzolite			2.6
Van7-85-49	Abyssal	SWIR	Lherzolite			2.0
Van7-96-09V	Abyssal	SWIR	Pyx Vn			6.4
Van7-96-18V	Abyssal	SWIR	Pyx Vn in Perid			25.2
Van7-96-21M	Abyssal	SWIR	Harz with Pyx Vn			3.3
Van7-96-21V	Abyssal	SWIR	Pyx Vn in Harz			2.5
Van7-96-25	Abyssal	SWIR	Lherzolite			22.2
Van7-96-28	Abyssal	SWIR	Lherzolite			5.0
Van7-96-35	Abyssal	SWIR	Lherzolite			4.8
Van7-96-38	Abyssal	SWIR	Lherzolite			5.7
HLY0102-40-81	Abyssal	Gakkel	Harzburgite	0.02		
PS59-235-17	Abyssal	Gakkel	Lherzolite			2.5
7TOW-57-4	Abyssal	Tonga Trench	Harzburgite	0.03	0.01	2.8
BMRG08-98-2-1	Abyssal	Tonga Trench	Harzburgite	0.04		
LS-33	Xenolith	Pali Aike	Gt Lherz	0.06	0.03	2.1
TMO	Xenolith	Pali Aike	Gt-Sp Lherz	0.03	0.01	2.3
SAV-AS1	Xenolith	Spitsbergen	Lherzolite	0.02	0.01	1.9
SAV-AS2	Xenolith	Spitsbergen	Lherzolite	0.04	0.02	2.2
SA-3-9	Xenolith	Samoa	Harzburgite	0.04		
3923J01	Orogenic	Josephine	Harzburgite	0.06		
3924J08	Orogenic	Josephine	Harzburgite	0.03		
3925G01	Orogenic	Josephine	Harzburgite	0.03		
JP08PS01	Orogenic	Josephine	Harzburgite	0.03	0.02	1.8
Average (excluding Van7-96)				0.04	0.02	2.4
Standard deviation				0.01	0.01	0.4
N				12	6	11

Experiments suggest that H diffusion decreases by approximately 2 orders of magnitude at low Fe contents, but that this difference disappears with increasing Fe [*Hercule and Ingrin*, 1999; *Woods et al*., 2000; *Stalder et al*., 2007; *Sundvall et al*., 2009].

In addition to Fe content, the movement of cations such as Al or Cr may also be rate limiting for dehydration. For example, significant amounts of hydrogen incorporation in pyroxene can occur by the coupled exchanges of (i) $^{IV}Al^{3+}$ and H^+ for Si^{4+} [*Skogby et al*., 1990; *Rauch and Keppler*, 2002; *Stalder and Skogby*, 2002; *Kohn et al*., 2005; *Hauri et al*., 2006; *Skogby*, 2006; *Karato*, 2008] and (ii) $^{VI}Al^{3+}$ and H^+ for $2Mg^{2+}$ [*Carpenter*, 2003; *Stalder and Skogby*, 2002; *Stalder*, 2004; *Kohn et al*., 2005]. Cpx in this study contains 2–8 wt % Al_2O_3 and Opx contains 2–6 wt % Al_2O_3, so Al-coupled mechanisms for hydrogen incorporation/extraction should be important.

In the absence of pyroxene diffusion data over a large range of pressures, fugacities, and compositions, we suggest that retention of H in pyroxenes may be largely due to cation-limited diffusion. Many studies of H diffusion in NAMs have identified both fast and slow diffusion processes, with fast diffusion typically occurring by the exchange of protons with electron holes [e.g., *Kohlstedt and Mackwell*, 1998, 1999]. Hence, the possibility remains that some fraction of water is lost very quickly from pyroxenes (and olivines), but that the majority is left behind in the case of pyroxenes. Our samples represent a wide range of tectonic environments (ocean ridges, subduction zones), surface exposures (subaerial to submarine), and exhumation rates (orogenic uplift, volcanic eruption), yet all have the same features of homogeneous pyroxenes and variably dehydrated olivines. Unless exhumation rates and accompanying evolutions in water fugacity coincidentally produced this set of data, we find it unlikely that such variety would not produce obvious differences with respect to tectonic setting, surface exposure, or mode of peridotite delivery to the surface.

5.4. Olivine-Pyroxene Partition Coefficients

The amount of water in olivine at mantle conditions is necessary for calculating mantle properties such as bulk mantle water content and viscosity. The original amount of water in olivine can be determined from either the Opx or Cpx water concentration if the mineral-mineral partition coefficient is known.

Estimates for partition coefficients between olivine, Opx, and Cpx are shown in Figure 6. For samples in this study, $D_{H_2O}^{Ol/Opx}$ has a range of 0.01–0.06 (Table 5), with an average value of 0.04 ± 0.01 ($N = 12$ samples), while $D_{H_2O}^{Ol/Cpx}$ has a range of 0.01–0.03, with an average of 0.02 ± 0.01 ($N = 6$). These values are relatively low, which is assumed to be due to water loss from olivine. For comparison, the xenolith average is $D_{H_2O}^{Ol/Opx} = 0.11 \pm 0.10$ ($N = 71$) and $D_{H_2O}^{Ol/Cpx} = 0.05 \pm 0.06$ ($N = 65$), based on a literature compilation [*Bell and Rossman*, 1992; *Peslier et al*., 2002; *Demouchy et al*., 2006; *Peslier and Luhr*, 2006; *Aubaud et al*., 2007; *Grant et al*., 2007b; *Falus et al*., 2008; *Li et al*., 2008; *Yang et al*., 2008; *Bonadiman et al*., 2009; *Xia et al*., 2010]. The large standard deviation for the average xenolith partition coefficients may be partly due to variations in FTIR data reduction methodologies and the inclusion of partially degassed olivines in the data set. *Hirth and Kohlstedt* [1996] estimated $D_{H_2O}^{Ol/Opx} = 0.2$ and $D_{H_2O}^{Ol/Cpx} = 0.1$, based on a combination of available data from natural and experimental samples.

Experimental data provide a better estimate of olivine-pyroxene partition coefficients, as experiments are cooled fast enough that loss of water from olivine—at least by the metal vacancy exchange mechanism—does not occur. Water partition coefficients vary as a function of pressure and Al content [e.g., *Hauri et al*., 2006; *Ardia et al*., 2012]. Current estimates from low-pressure (<2 GPa) alumina-bearing experiments analyzed by SIMS are $D_{H_2O}^{Ol/Opx} = 0.11 \pm 0.03$ ($N = 12$) and $D_{H_2O}^{Ol/Cpx} = 0.07 \pm 0.02$ ($N = 9$) (Figure 6, using data from *Aubaud et al*. [2004], *Hauri et al*. [2006], and *Tenner et al*. [2009]). Additional $D_{H_2O}^{Ol/Opx}$ experimental data are available in *Grant et al*. [2006, 2007a], with $D_{H_2O}^{Ol/Opx} = 0.34 \pm 0.21$ based on nine experiments, of which seven are nominally alumina free. The Grant data sets were collected by FTIR and plot significantly off the trend of the other experimental data sets. This difference may reflect uncertainties in the baseline correction, as discussed by *Grant et al*. [2006], and in the absorption coefficients used to convert FTIR spectra into absolute water concentrations, which have undergone revisions in recent years [*Withers et al*., 2012; *Mosenfelder and Rossman*, 2013a]. Hence, the Grant data are excluded from the average values for olivine-pyroxene partitioning. In addition, partition coefficients should vary as a function of temperature, oxidation state, and water fugacity [*Dai and Karato*, 2009], but data are not available to constrain these effects. Using the low-pressure alumina-bearing experiments, the best available experimental estimate for $D_{H_2O}^{Ol/Opx}$ is 0.11. We use this value below to calculate high-temperature olivine water concentrations based on Opx water concentrations.

5.5. Cpx-Opx Partition Coefficients

The partition coefficient between Cpx and Opx has an average value in this study of $D_{H_2O}^{Cpx/Opx} = 2.4 \pm 0.3$ ($N = 11$), excluding SWIR veined peridotites (Table 5). In Figure 6, our data set is compared to published data sets for pyroxenes in experiments and xenoliths. Alumina-bearing experimental data give $D_{H_2O}^{Cpx/Opx} = 1.3 \pm 0.3$ ($N = 10$) [*Aubaud et al*., 2004; *Hauri et al*., 2006; *Tenner et al*., 2009]. The larger number of published xenolith analyses gives $D_{H_2O}^{Cpx/Opx} = 2.6 \pm 0.9$ ($N = 141$), in agreement with results of this study. The combined value for natural samples (literature data plus our data) is $D_{H_2O}^{Cpx/Opx} = 2.6 \pm 0.9$ ($N = 152$).

The two separate $D_{H_2O}^{Cpx/Opx}$ trends (Figure 6) when comparing experiments to natural samples suggest a systematic difference. The lower experimental value for Cpx/Opx partitioning could result from differences in major element compositions relative to natural pyroxenes. For example, the charge-coupled substitution of aluminum onto the silica tetrahedral site ($Si^{4+} = {}^{IV}Al^{3+} + H^{+}$) is one of the mechanisms for the incorporation of water into pyroxenes [e.g., *Rauch and Keppler*, 2002; *Kohn et al*., 2005]. However, in Figure 7, $D_{H_2O}^{Cpx/Opx}$ does not correlate with ${}^{IV}Al^{3+}$ in Opx or Cpx for natural samples. Experimentally determined values for $D_{H_2O}^{Cpx/Opx}$ show only a weak correlation with Opx ${}^{IV}Al^{3+}$ and no correlation with Cpx ${}^{IV}Al^{3+}$. The proportion of ${}^{IV}Al^{3+}$ on tetrahedral sites in Opx versus Cpx is similar in both experiments and natural samples (Figure 7c). In contrast, experiments contain less Cr^{3+} on the M1 site in Cpx compared to Opx (Figure 7d). Experimental Cpx also have more Fe^{2+} on the M2 site when compared to Opx (Figure 7e), but systematic differences are not observed for Fe^{2+} on the M1 site and for Fe^{3+} on either site. Other cations, such as Ti^{4+}, do not show any systematic offset between experiments and natural samples. The difference in Cr^{3+} and Fe^{2+} may explain the slightly higher value for $D_{H_2O}^{Cpx/Opx}$ in natural samples in comparison to experiments. However, caution is necessary in using Fe

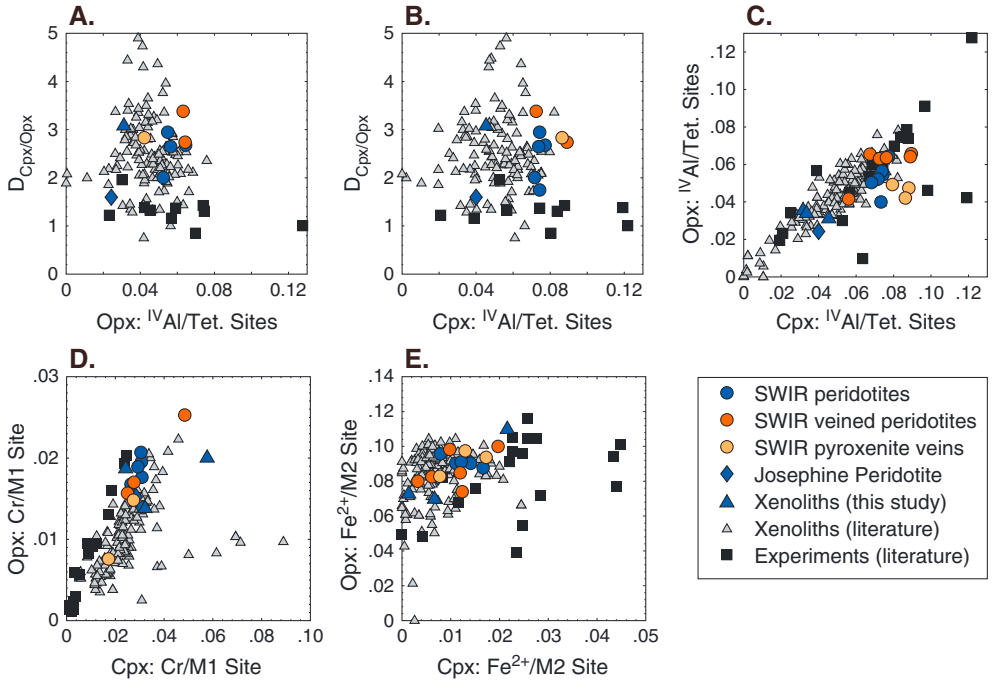

Figure 7. (a) Variation of $D_{H_2O}^{Cpx/Opx}$ as a function of $^{IV}Al^{3+}$ content in Opx. Experiments show a weak partition coefficient dependence on $^{IV}Al^{3+}$, whereas natural samples do not. (b) Variation of $D_{H_2O}^{Cpx/Opx}$ as a function of $^{IV}Al^{3+}$ content in Cpx. Systematic variations do not occur among experiments or natural samples. (c) Variation in $^{IV}Al^{3+}$ as a proportion of the pyroxene tetrahedral sites. Experiments and natural samples have similar amounts of $^{IV}Al^{3+}$ in both Opx and Cpx. Other cations (e.g., Ti^{4+}, Fe^{3+}) show similar variations. (d) Variation in Cr^{3+} as a proportion of the M1 site. Experiments have relatively more Cr^{3+} in Opx compared to Cpx. (e) Variation in Fe^{2+} as a proportion of the M2 site. Experiments have relatively less Fe^{2+} in Opx compared to Cpx. Mineral microprobe data for our samples are from *Stern et al.* [1989], *Hauri and Hart* [1994], *Warren et al.* [2009], and *Skemer et al.* [2010]. Site occupancies were calculated from microprobe data assuming perfect stoichiometry, with data and calculated components provided in Table S4. References for literature data are in Figure 2 for xenoliths and Figure 6 for experiments.

speciation and site occupancy that is only constrained by electron microprobe data. *Dyar et al.* [1989] have shown that Mössbauer analysis is necessary to fully constrain this in pyroxenes.

Other possible causes of the difference between experimental and natural $D_{H_2O}^{Cpx/Opx}$ are (i) differences in total water content, (ii) differences in temperature and cooling rate between the two systems, and (iii) differences in oxygen fugacity. Although most experiments were H_2O undersaturated, the H_2O fugacity is probably higher than that for natural samples, as indicated in Figure 6 by higher water concentrations in experimental pyroxenes. If there is more than one H substitution mechanism (e.g., coupled $^{IV}Al^{3+}$ substitution and coupled metal vacancy substitution), these could have different dependencies on total water fugacity. While experimental data do not show evidence for this [*Hauri et al.*, 2006], such a dependency is required in thermodynamic models for water solubility in pyroxenes under water-saturated conditions [*Keppler and Bolfan-Casanova*, 2006]. Higher Fe^{3+} in experimental pyroxenes relative to natural pyroxenes could also drive differences in $D_{H_2O}^{Cpx/Opx}$. When buffered, experiments are typically conducted around Ni-NiO, whereas the mantle has an oxygen fugacity near the quartz-fayalite-magnetite buffer [*Wood et al.*, 1990]. The influence of Fe^{3+} on partitioning has not been examined experimentally and is thus unconstrained.

Pyroxenites and pyroxenite-veined peridotites from dredge Van7-96 plot off the Cpx/Opx partitioning trend in Figure 6. Cpx and Opx in two samples appear to be in disequilibrium, with $D_{H_2O}^{Cpx/Opx} > 20$. Among the other veined samples, $D_{H_2O}^{Cpx/Opx} = 4.6 \pm 1.5$ ($N = 6$), which is significantly higher than the partition coefficient for unveined samples. The higher $D_{H_2O}^{Cpx/Opx}$ in pyroxenitic samples may be due to higher Cpx aluminum contents, incomplete equilibration during formation of the pyroxenite veins, or differences in oxygen fugacity.

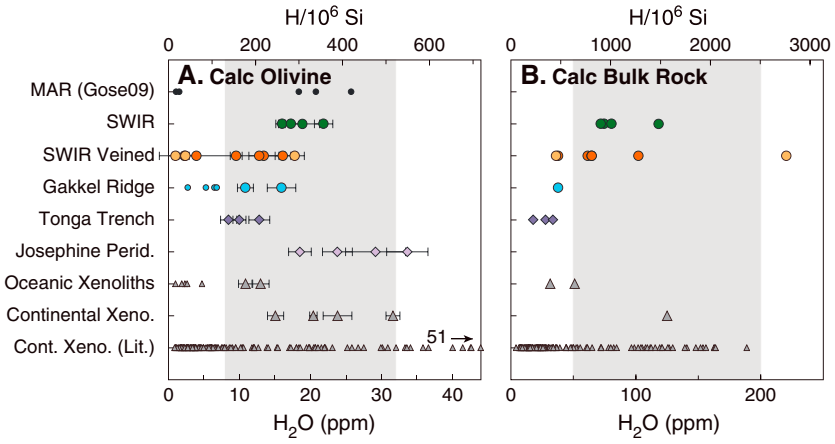

Figure 8. (a) Calculated water concentrations in olivine, based on Opx water concentrations and assuming $D_{H_2O}^{Ol/Opx} = 0.11$. Error bars indicate 2σ standard deviations in the average of multiple analyses per sample. (b) Calculated bulk peridotite water concentrations for samples that have measured mineral modes. Smaller symbols indicate literature data (see Figure 2 for references). Grey shaded fields are estimated water concentration ranges for the upper mantle (see Table 3 for details).

5.6. Bulk Mantle Water Concentrations

Bulk mantle water contents can be estimated using the modal abundances of upper mantle minerals, measured water concentrations, and partition coefficients (Figure 6). For the calculation, olivine water concentrations were estimated assuming $D_{H_2O}^{Ol/Opx} = 0.11$, which is the average value from low-pressure alumina-bearing experiments [*Aubaud et al*., 2004; *Hauri et al*., 2006; *Tenner et al*., 2009]. For five samples without measured Cpx water concentrations (of which three contain <1% modal Cpx), values were estimated assuming $D_{H_2O}^{Cpx/Opx} = 2.6$, which is the average value from xenoliths in the literature (see Figure 2 for references).

Variations in calculated water concentrations for olivine and bulk rock peridotites are shown in Figure 8. Calculated olivine concentrations range from 8 to 34 ppm H_2O for samples in this study (Table 6) and from 1 to 51 ppm for xenoliths from the literature. Calculated olivine concentrations are within a reasonable range compared to estimates of upper mantle olivine (8–32 ppm; Table 3). However, concentrations in ridge peridotites are higher than predicted for the residues of melting, which is discussed in detail in the next section.

The range of calculated bulk rock concentrations for samples in this study is 18–220 ppm H_2O (Table 6), which compares favorably to the pre-melting upper mantle range of 50–200 ppm H_2O [*Hirschmann*, 2006]. Unveined abyssal peridotites contain 18–118 ppm, while the Pali Aike continental xenolith has 125 ppm and the Samoa oceanic xenoliths have 31–51 ppm. SWIR pyroxenite-veins cover the largest range of water concentrations, from 36 to 220 ppm, due to the abundance of pyroxene in these samples and the large variation in pyroxene water contents (9–162 ppm in Opx).

Calculated bulk water concentrations are plotted as a function of peridotite depletion in Figure 9. Cpx mode and bulk Al_2O_3 both decrease during melting, while spinel Cr# increases during melting. Our data suggest that bulk water concentrations are correlated with the degree of peridotite depletion. Among unveined abyssal peridotites, bulk water concentrations have correlation coefficients of 0.99 with modal Cpx, 0.94 with bulk Al_2O_3, and −0.97 with spinel Cr#. Xenoliths in this study also plot on these trends, though they are not included in the regressions in Figure 9. The correlation between bulk water and modal Cpx is not simply due to Cpx modal abundance: Although Cpx has an average of 2.6 times more water than Opx, Opx is 2–10 times more abundant than Cpx, and there is no correlation between Opx and Cpx modes.

We also calculated bulk peridotite water concentrations for published xenolith data sets for which modal data are available (143 samples; Figure 9). In studies by *Peslier et al*. [2002] and *Peslier and Luhr* [2006], bulk water is weakly correlated with Cpx mode, bulk Al_2O_3, and spinel Cr# ($r = 0.88$, 0.73, −0.70, respectively). Other xenolith data sets show no correlation. These samples are mainly continental xenoliths, so the lack of systematic variations may reflect various episodes of melt and fluid refertilization [e.g., *Peslier*, 2010].

Table 6. Peridotite Compositions and Calculated Variables

		Measured[a]								Calculated			
Sample	Location	Bulk Al_2O_3 wt %	Spin Cr#	Cpx Ce ppm	Modes Oliv	Opx	Cpx	Spin	Gt	Oliv H_2O[b] ppm	Bulk H_2O[c] ppm	Bulk Ce[d] ppm	Effective Viscosity[e] Pa s
PS86-6-38	SWIR	3.50	11.26	0.57	0.57	0.29	0.13	0.02		19	118	0.077	1.2E + 20
Van7-85-42	SWIR	2.28	15.91	0.02	0.67	0.26	0.06	0.01		16	75	0.002	1.4E + 20
Van7-85-47	SWIR	2.45	17.40	0.01	0.69	0.25	0.05	0.01		17	72	0.001	1.3E + 20
Van7-85-49	SWIR	1.84	14.95	0.03	0.72	0.22	0.05	0.01		22	81	0.002	9.9E + 19
Van7-96-09V	SWIR	8.79	34.44	1.56	0.11	0.30	0.57	0.02		1	36	0.904	2.5E + 21
Van7-96-18M	SWIR	2.97	10.19	1.87						4			7.7E + 20
Van7-96-18V	SWIR	8.27	16.02	1.49						2			2.5E + 21
Van7-96-21M	SWIR	2.37	26.54	5.13	0.77	0.18	0.05	0.01		16	62	0.273	1.4E + 20
Van7-96-21V	SWIR	4.87	16.61	5.28	0.20	0.40	0.38	0.02		18	220	2.080	1.3E + 20
Van7-96-25	SWIR	2.52	13.75	1.44	0.66	0.26	0.07	0.01		2	38	0.111	2.5E + 21
Van7-96-28	SWIR	2.42	32.33	4.00	0.77	0.17	0.05	0.01		13	65	0.242	1.8E + 20
Van7-96-35	SWIR	1.42	23.96	2.21	0.71	0.17	0.11	0.02		10	65	0.246	2.7E + 20
Van7-96-38	SWIR	4.10	11.50	0.96	0.64	0.24	0.10	0.02		13	102	0.103	1.9E + 20
HLY0102-40-81	Gakkel	0.98			0.68	0.30	0.00	0.01		11	38		2.3E + 20
PS59-235-17	Gakkel			0.24						16			1.4E + 20
7TOW-57-4	Tonga Trench	0.52		0.02	0.80	0.18	0.01	0.00		10	28	0.0003	2.5E + 20
BMRG08-98-2-1	Tonga Trench	0.42	58.36		0.85	0.14	0.00	0.01		8	18		3.1E + 20
NOVA-88-A1	Tonga Trench			0.07	0.79	0.20	0.00	0.01		13	34	0.0006	1.9E + 20
LS-33	Pali Aike	3.43		4.54	0.55	0.20	0.15		0.10	24	125		8.9E + 19
TMO	Pali Aike	2.86		4.52						32			6.3E + 19
SAV-AS1	Spitsbergen			22						20			1.1E + 20
SAV-AS2	Spitsbergen			7.38						15			1.5E + 20
SA-3-9	Samoa		47.20	0.20	0.77	0.22	0.01	0.01		11	31	0.003	2.3E + 20
SAV-1-28	Samoa	1.34	37.80	112	0.68	0.28	0.03	0.01		13	51	4.565	1.8E + 20
3923J01	Josephine									19			1.2E + 20
3924J08	Josephine									24			8.9E + 19
3925G01	Josephine									34			5.9E + 19
JP08PS01	Josephine			0.01						29			7.0E + 19

[a]Compositional data for SWIR samples from *Warren et al*. [2009] and *Craddock et al*. [2013]; for Pali Aike from *Stern et al*. [1989, 1999]; for Samoa from *Hauri et al*. [1993] and *Hauri and Hart* [1994].

[b]Calculated olivine H_2O concentrations from Opx H_2O concentrations, assuming $D^{Ol/Opx} = 0.11$.

[c]Spinel and garnet are excluded from the bulk concentration calculation due to the very low abundance of water in these minerals, along with the low modal abundance of spinel.

[d]Bulk Ce concentrations are calculated from measured Cpx Ce concentrations and mineral modes, using the formulation in *Workman and Hart* [2005] and Ce mineral/melt partition coefficients from *Kelemen et al*. [2003].

[e]Effective viscosity, calculated as a function of olivine water content, at a temperature of 1200°C, pressure of 0.5 GPa, and shear stress of 0.3 MPa. See section 5.9 for details.

Alternatively, the lack of strong correlations may reflect uncertainties in FTIR data reduction, including the choice of calibration, baseline fitting of spectra, and effects of cracks, alteration, and microscopic inclusions [e.g., *Bell et al*., 2003; *Aubaud et al*., 2009; *Kovács et al*., 2010; *Stalder et al*., 2012; *Mosenfelder and Rossman*, 2013a, 2013b; *Withers*, 2013].

5.7. Variation of H_2O and Ce in Peridotites

The trace element Ce is used as a proxy for water concentration in basalts, as the relatively constant H_2O/Ce ratio in mid-ocean ridge basalts (MORBs) suggests similar partitioning during melting [*Michael*, 1995]. Estimates for the amount of water in the upper mantle are based on the H_2O/Ce ratio, which has a range of 150–250 in basalts [*Michael*, 1995; *Saal et al*., 2002], combined with estimates of upper mantle Ce (0.4–0.7 ppm) [*Salters and Stracke*, 2004; *Workman and Hart*, 2005]. The MORB source is thus estimated to have 50–200 ppm H_2O, while ocean island basalt mantle is estimated to have 100–300 ppm H_2O [*Hirschmann*, 2006]. In Figure 10, estimates for H_2O and Ce in the MORB mantle source are shown as grey shaded fields.

Peridotites show a considerable range of H_2O/Ce ratios, at both the mineral level (Figure 10a) and the bulk rock level (Figure 10b). To explore the implications of H_2O-Ce variations in peridotites, we ran nonmodal

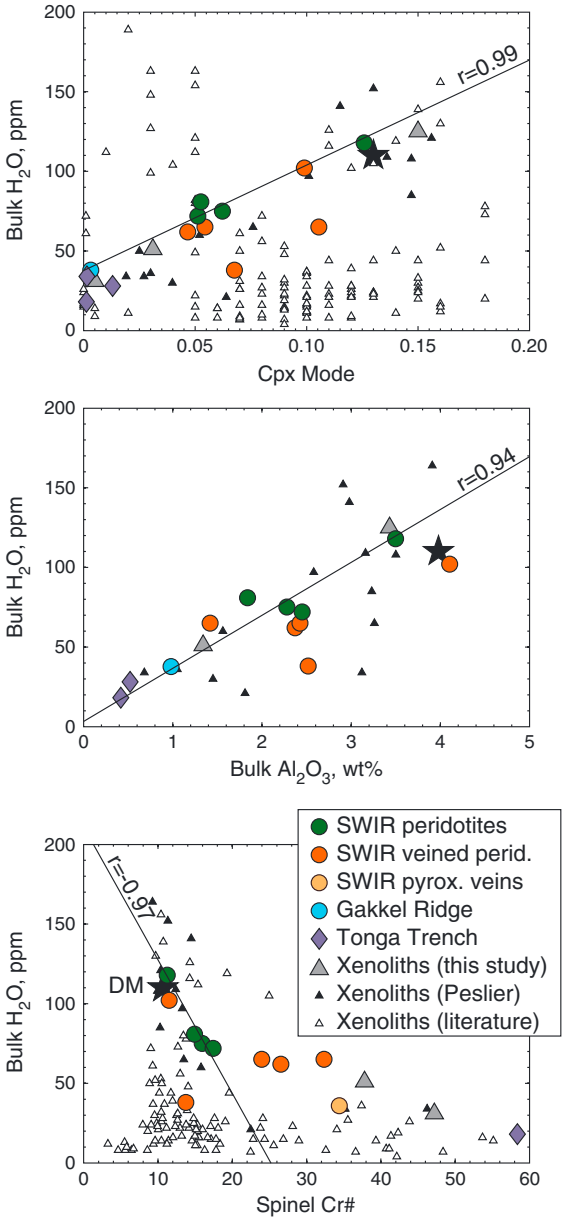

Figure 9. Variations in bulk peridotite water concentrations as a function of peridotite proxies for degree of melting. Solid lines are least squares regressions through the unveined ridge peridotites in this study, for which Cpx mode, bulk Al_2O_3, and spinel Cr# are given in Table 6. References for literature xenoliths are given in Figure 2. The model composition of the source-depleted mantle (DM, black star) is from *Workman and Hart* [2005].

fractional and dynamic melting models (Figure 11). As a first step, the degree of melting represented by abyssal peridotite REE concentrations was modeled using equations from *Zou* [1998], an initial mantle composition from *Workman and Hart* [2005], and melting reactions as referenced in Table 7. Bulk rock REE concentrations (Figure 11a) were calculated from Cpx trace element concentrations using mineral-mineral partition coefficients [*Kelemen et al.*, 2003] and mineral modes. For SWIR samples, REE patterns can be reproduced by ~1–6% melting in the spinel field using either fractional or dynamic melting models. For dynamic melting, a fit was obtained using a residual porosity (φ) of 0.1%, with larger porosity values yielding worse fits.

In contrast to SWIR samples, the Tonga Trench peridotites are difficult to fit using either fractional or dynamic melting models. While heavy REEs can be reproduced by ~12.5% melting, light REEs have concentrations that are too high to be fit, even at high values of φ (~2%). Tonga peridotites are overall more complicated than ridge peridotites, as indicated by spinel Cr# >60 and bulk rock $Al_2O_3 < 1$ wt %. These chemical characteristics suggest a melting history that possibly involved fluxing by melt and fluids in the subduction zone.

Using estimates for degree of melting from the REE modeling of SWIR samples, the variation in bulk peridotite Ce and H_2O was modeled (Figure 11b). As the difference between dynamic and fractional melting models is small, only the fractional model was used to explore variations in H_2O during melting. Various sets of H_2O partition coefficients were tested in the model, as published partition coefficients (Table 7) are not internally consistent: i.e., $D_{H_2O}^{Cpx/Melt}/D_{H_2O}^{Opx/Melt} \neq D_{H_2O}^{Cpx/Opx}$, etc. This discrepancy is likely due to the difficulty of running multiply saturated experiments, meaning that H_2O activities are not the same as that imposed by the full peridotite assemblage. To overcome the inconsistency among partition coefficients, we calculated $D_{H_2O}^{Min/Melt}$ for Cpx and olivine based on $D_{H_2O}^{Opx/Melt} = 0.018$ [*O'Leary et al.*, 2010], $D_{H_2O}^{Ol/Opx} = 0.11$, and $D_{H_2O}^{Cpx/Opx} = 2.6$. Spinel was assumed to contain no water and was excluded from the calculations. Using different published values for the partition coefficients [*Aubaud et al.*, 2004; *Hauri et al.*, 2006; *Kohn and Grant*, 2006; *Grant et al.*, 2007a; *Hirschmann et al.*, 2009; *Tenner et al.*, 2009] results in small variations among the modeled trajectories of the melt residues.

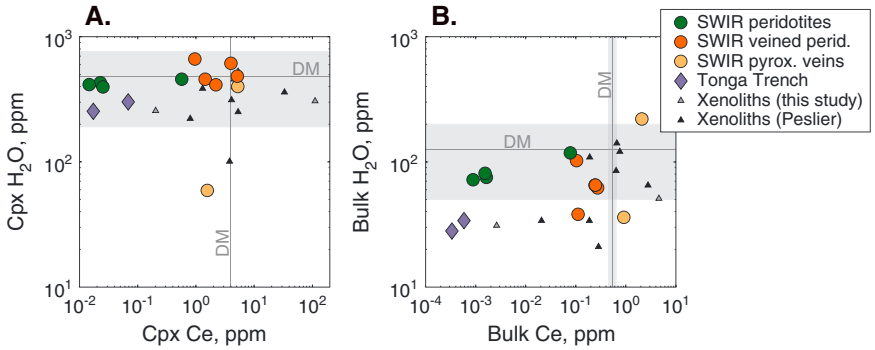

Figure 10. (a) Variation of measured water concentrations in Cpx compared to measured Cpx Ce concentrations. (b) Variation of calculated bulk H_2O concentrations as a function of calculated bulk Ce concentrations. For comparison, data from the xenolith study by *Peslier et al.* [2002] are shown. Bulk Ce concentrations are calculated from measured Cpx Ce concentrations using mineral modes (Table 6) and Ce mineral/melt partition coefficients (Table 7). The average estimated concentrations of upper mantle H_2O [*Hirschmann*, 2006] and Ce [*Workman and Hart*, 2005] are shown as grey lines, with the grey boxes indicating the ranges of these estimates. The concentration of H_2O in upper mantle Cpx (190–760 ppm) is calculated from the bulk mantle estimate (see Table 3 for details).

The fractional melting model in Figure 11b reproduces the H_2O-Ce trend of MORB data along a trajectory of 1–6% melting. The MORB data are slightly offset from the model and a better fit could be achieved by fine tuning the partition coefficient values and model parameters. However, more significant is the complete mismatch between the trajectory of the melt residue and the peridotite H_2O-Ce data set. To produce a match would require $D_{H_2O}^{Bulk/Melt} > D_{Ce}^{Bulk/Melt}$, whereas MORB and experimental studies have found $D_{H_2O}^{Bulk/Melt} < D_{Ce}^{Bulk/Melt}$ (Table 7). Furthermore, any set of partition coefficients that reproduces the peridotite data is not able to simultaneously match MORB compositions, regardless of the degree of melting used in the model.

The fractional melting model indicates that the amount of water in abyssal peridotites is higher than expected for residues of melting. However, instantaneous melts in equilibrium with peridotites have reasonable water concentrations. The most depleted peridotite (BMRG08-98-2-1) has 18 ppm H_2O and

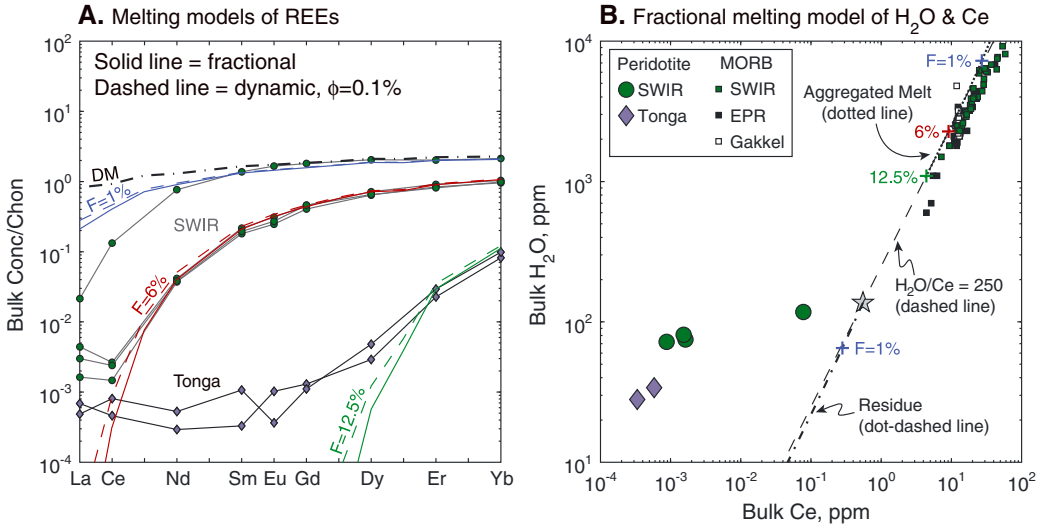

Figure 11. (a) Results of REE modeling of spinel field melting for bulk rock abyssal peridotites. Fractional and dynamic non-modal melting models give similar results; for simplicity, only the fractional melting model is shown in Figure 11b. (b) The evolution of peridotite residue and aggregated melt for Ce and H_2O during fractional melting, using partition coefficients given in Table 7. Also shown are published H_2O-Ce data sets for MORBs [*le Roux et al.*, 2006; *Standish*, 2006; *Standish et al.*, 2008; *Shaw et al.*, 2010]. The melting model fits the basalt data (dotted line) but completely misses the peridotite data (dash-dotted line). In addition, the basalt data align along a line of constant H_2O-Ce ratio (dashed line), whereas the peridotite data plot far from this line.

Table 7. Parameters Used for Modeling Trace Elements[a]

Partition Coefficient	Oliv/Melt	Ref	Opx/Melt	Ref	Cpx/Melt	Ref	Bulk/Melt	Ref
Published Values for Partition Coefficients								
D_{H2O}	0.0014	1	0.018	1, 2	0.010	1, 2	0.007–0.009	1, 3
D_{Ce}	0.00001	4	0.003	4	0.0858	5	0.012–0.022	4, 6
D_{H2O}/D_{Ce}	140		6		0.1		0.3–0.4	
Internally Consistent Values for D_{H2O}, Based On $D^{Opx/Melt} = 0.018$, $D^{Ol/Opx} = 0.11$, and $D^{Cpx/Opx} = 2.6$								
D_{H2O}	0.002	calc.	0.018	1, 2	0.047	calc.	0.012	calc.
D_{H2O}/D_{Ce}	200		6		0.5		0.6–1.0	
Modes	Olivine	Ref	Opx	Ref.	Cpx	Ref	Spinel	Ref
Source modes	0.57	6	0.28	6	0.13	6	0.02	6
Melt modes	−0.06	7	0.28	7	0.67	7	0.11	7

[a]References: 1 = *Hauri et al.* [2006]; 2 = *O'Leary et al.* [2010], assuming pyroxene $^{IV}Al^{3+} = 0.04–0.07$; 3 = *Hirschmann* [2006]; 4 = *Kelemen et al.* [2003]; 5 = *Hart and Dunn* [1993]; 6 = *Workman and Hart* [2005]; 7 = *Kinzler* [1997].

$D_{H_2O}^{Bulk/Melt} = 0.004$ (calculated from mineral modes and mineral/melt partition coefficients), which corresponds to an equilibrium melt with 0.45 wt % H_2O. The most enriched unveined abyssal peridotite (PS86-6-38) has 118 ppm H_2O and $D_{H_2O}^{Bulk/Melt} = 0.012$, which corresponds to an equilibrium melt with 1 wt % H_2O. For comparison, MORB glasses have ~0.1–1.5 wt % H_2O [*Dixon et al.*, 2002]. The similarity between MORB water concentrations and instantaneous melts in equilibrium with peridotites suggests that peridotite compositions may reflect equilibration with late-stage melts trapped in the shallow mantle. Open-system melting and refertilization have often been invoked to explain concentrations of the light REEs in abyssal and orogenic peridotites [e.g., *Godard et al.*, 1995, 2008; *Ozawa and Shimizu*, 1995; *Vernières et al.*, 1997; *Warren et al.*, 2009]. This same mechanism may have resulted in the relatively high water content of abyssal peridotites, which would account for the high apparent $D_{H_2O}^{Bulk/Melt}$ suggested by these peridotites.

If the high water contents of abyssal peridotites are due to late-stage refertilization, this implies that the percolating melt has relatively low Ce (and other REE) concentrations. A high water/low Ce melt does not match many natural magmas, particularly in a ridge setting. However, if a late-stage melt infiltrated peridotite at relatively low temperature, diffusion of H may have been fast enough for reequilibration while other trace elements diffused too slowly to equilibrate. For example, REEs have pyroxene diffusion coefficients $<10^{-22}$ m^2/s at 1000°C [*Van Orman et al.*, 2001; *Cherniak and Liang*, 2007; *Cherniak and Dimanov*, 2010], which is orders of magnitude slower than H diffusion at this temperature.

An alternative explanation for the relatively high water contents in abyssal peridotites is that partition coefficients used in the model do not reflect partitioning throughout the melting process [e.g., *Kohn and Grant*, 2006]. In fact, the constant H_2O/Ce ratio in basalts is somewhat surprising given their different mineral hosts in the mantle. In spinel peridotites, the majority of Ce is hosted in Cpx, whereas significant amounts of water are hosted in olivine and Opx in addition to Cpx. This is reflected in the mineral/melt partition coefficients for Ce and H_2O, which demonstrate differences on a mineral-by-mineral basis (Table 7): e.g., $D_{H_2O}^{Cpx/Melt} < D_{Ce}^{Cpx/Melt}$, but $D_{H_2O}^{Ol/Melt} > D_{Ce}^{Ol/Melt}$ [*Kohn and Grant*, 2006]. Furthermore, water partitioning varies as a function of pressure, water activity, mineral modes, and Al_2O_3 content [*Hirth and Kohlstedt*, 1996; *Asimow et al.*, 2004; *Hauri et al.*, 2006; *Tenner et al.*, 2009, 2012; *Ardia et al.*, 2012]. For example, *Hauri et al.* [2006] estimated that $D_{H_2O}^{Bulk/Melt} \approx D_{Ce}^{Bulk/Melt}$ in the spinel peridotite field but $D_{H_2O}^{Bulk/Melt} < D_{Ce}^{Bulk/Melt}$ for melting above 4 GPa in the garnet lherzolite field. At higher Al_2O_3 contents, pyroxenes have higher values of $D_{H_2O}^{Pyx/Melt}$ [e.g., *Grant et al.*, 2007a; *O'Leary et al.*, 2010]. Hence, $D_{H_2O}^{Bulk/Melt}$ may initially be higher than current estimates due to the higher Al_2O_3 content of pyroxenes in fertile mantle. As H_2O and Ce are incompatible elements, peridotites should be sensitive to these effects and potentially record larger ranges of H_2O/Ce ratios than are observed in aggregated MORB melts.

The relationship between water and Ce in our data set is based on a limited number of samples and may also reflect regional variations in upper mantle composition. Additional peridotite analyses are necessary to fully

explore the H_2O-Ce relationship, as well as the systematics observed with other proxies for degree of melting (e.g., Figure 9).

5.8. Variations in Water Content by Tectonic Setting

Depending on tectonic setting, the estimated bulk water concentration of measured samples varies: ridges, Tonga Trench, and oceanic xenoliths have lower concentrations than continental xenoliths and the Josephine Peridotite (Figures 2 and 8). Abyssal peridotites have a range of water concentrations, with Gakkel Ridge and MAR peridotites extending to lower water concentrations than SWIR unveined peridotites. The lower water content of Gakkel compared to SWIR is also observed among basalts, as Gakkel basalts have 0.26 ± 0.04 wt % H_2O [*Shaw et al*., 2010] compared to 0.60 ± 0.20 wt % H_2O in SWIR basalts [*Standish et al*., 2008]. However, any detailed comparison of ridge-scale variations requires analysis of larger sample suites from these regions. Similarly, the variation among continental xenoliths (137–287 ppm H_2O in Opx) in our sample set is smaller than the literature range for xenoliths (8–460 ppm), but this reflects the limited number of locations investigated.

Despite limited sampling, some aspects of the present data set are significant in the context of tectonic setting. The first is the contrast in water contents of the two subduction zone sample suites. Specifically, Tonga peridotites have very low water contents (77–116 ppm H_2O in Opx), whereas Josephine peridotites have the highest water contents (168–289 ppm) of samples in this study (Figure 2). Tonga peridotites were collected at the bottom of the Tonga trench from the Australian Plate, which is overriding the subducting Pacific Plate [*Bloomer and Fisher*, 1987; *Wright et al*., 2000]. These peridotites thus represent mantle from the fore-arc region of a subduction zone, which is typically more compositionally depleted than both mid-ocean ridge and back-arc mantle [*Arai and Ishimaru*, 2007]. In contrast, the Josephine Peridotite is suggested to have originated in either a fore-arc [*Dick*, 1976; *Kelemen et al*., 1995] or back-arc setting [*Harper*, 1984]. The relatively high water content of the Josephine would favor a back arc, though other trace elements are not similarly enriched (Figure 4).

The Josephine Peridotite samples have high, but variable, water concentrations, which is important as the principal slip system in olivine changes as a function of water content and shear stress [*Jung and Karato*, 2001; *Jung et al*., 2006]. At low shear stress, olivine undergoes a transition in slip system around 30 ppm H_2O (500 ppm H/Si), based on olivine deformation experiments [*Jung et al*., 2006] adjusted for the calibration of *Bell et al*. [2003]. At <30 ppm H_2O, olivine deforms principally by slip on the (010) plane in the [100] direction, which is referred to as Type-A slip or easy slip. At higher water concentrations, the principal slip system in olivine changes to the (001) plane in the [100] direction, which is referred to as Type-E slip. Most of the Josephine samples have calculated olivine water concentrations of <30 ppm, so Type-A slip is expected. However, sample 3925G02 has a high enough water concentration that a transition to Type-E slip is predicted. Lattice-preferred orientation analyses by *Warren et al*. [2008] and *Skemer et al*. [2010] confirm that the low (<30 ppm H_2O) concentration samples have Type-A olivine fabrics, while sample 3925G02 (with 34 ppm H_2O or 550 ppm H/Si) has a Type-E fabric. These samples are from high-temperature ductile shear zones [*Kelemen and Dick*, 1995] and increased water contents also correspond to outcrop-scale increases in shear strain. By modeling the effect of water on olivine deformation, *Skemer et al*. [2013] showed that elevated water contents promoted shear localization in these shear zones.

Variations in olivine water content in the mantle wedge of subduction zones have been proposed as a mechanism behind trench-parallel seismic anisotropy [e.g., *Jung and Karato*, 2001; *Kneller et al*., 2005; *Ohuchi et al*., 2012]. Tonga exhibits trench-parallel shear wave splitting in the 19–21°S region of the trench [*Smith et al*., 2001], which is the location of our samples. One possible explanation is that elevated water in the nose of the mantle wedge has resulted in a change in the olivine slip system, such that the olivine [100] axis is no longer aligned with the flow direction [*Jung and Karato*, 2001; *Kneller et al*., 2005]. However, this would require water concentrations in olivine that are >30 ppm H_2O (~500 ppm H/Si). As such high water contents are not observed in Tonga peridotites, other mechanisms must be responsible for the observed trench-parallel splitting, such as complex 3-D flow dynamics [e.g., *Long and Silver*, 2008].

The final notable aspect of the peridotite data set is the large range in water concentrations among pyroxenite-veined peridotites from SWIR dredge Van7-96. These peridotites and associated pyroxenite

veins do not have distinct water concentrations, nor are trace element and isotopic compositions different between vein and host peridotite [*Warren et al*., 2009]. For example, pyroxenite Opx has a concentration range of 9–162 ppm H_2O, while peridotite Opx has a range of 21–147 ppm. (Note that veined peridotites are too small for measurements to be made >10 cm from a vein.) For comparison, dredge Van7-85, located farther east along the ridge, has a more limited range of 145–198 ppm in peridotite Opx. Trace element and radiogenic isotopic compositions of dredge Van7-96 peridotites and pyroxenites have previously been taken as evidence for substantial melt addition to the mantle during passage of the Bouvet hot spot around 15 Ma [*Warren et al*., 2009; *Warren and Shirey*, 2012]. While plume material is generally estimated to have a water content of 300–1000 ppm, recycled subducted crust in plumes may have only ~60 ppm H_2O [*Nadeau et al*., 1993; *Dixon et al*., 2002]. Two of the three pyroxenites in this study have extremely low water concentrations of 9–22 ppm in Opx, which corresponds to ~36 H_2O ppm in the bulk pyroxenite. This supports the interpretation that some material in the Bouvet plume is derived from recycled oceanic crust.

5.9. Viscosity Variations

Olivine water concentrations can be used to predict effective viscosity variations in the mantle. Calculated olivine concentrations, based on Opx concentrations, range from 8 to 34 ppm H_2O (140–550 ppm H/Si) in unveined peridotites and from 1 to 18 ppm H_2O (16–290 ppm H/Si) in SWIR veined peridotites (Table 6). For comparison, xenoliths in the literature range from 1 to 51 ppm H_2O (16–830 ppm H/Si) in olivine, also calculated from Opx water concentrations.

Olivine in the upper mantle deforms by dislocation creep [e.g., *Goetze and Kohlstedt*, 1973; *Karato et al*., 1986; *Hirth and Kohlstedt*, 1995]. *Hirth and Kohlstedt* [2003] give the olivine dislocation creep flow law as

$$\dot{\varepsilon} = A\sigma^n C_{\mathrm{OH}}^r \exp\left(-\frac{E+PV}{RT}\right)$$

where $\dot{\varepsilon}$ is strain rate, A is a constant, σ is differential stress, n is the stress exponent, C_{OH} is water concentration in ppm H/Si, r is the water concentration exponent, E is activation energy, V is activation volume, and T is absolute temperature. For wet dislocation creep, $A = 30$ (where A has been adjusted for the FTIR calibration of *Bell et al*. [2003], assuming a correction factor of 2.5), $n = 3.5$, $r = 1.2$, $E = 480$ kJ/mol, and $V = 11 \times 10^{-6}$ m^3/mol [*Hirth and Kohlstedt*, 2003]. When olivine has <3 ppm H_2O (<50 ppm H/Si), the dry flow law is applicable as the concentration of hydrogen is too low for the charge neutrality condition to control the point defect population [*Mei and Kohlstedt*, 2000]. In the dry dislocation creep flow law, the C_{OH}^r term disappears, $A = 1.1 \times 10^5$, $n = 3.5$, $E = 530$ kJ/mol, and $V = 18 \times 10^{-6}$ m^3/mol [*Hirth and Kohlstedt*, 2003].

Effective viscosity can be calculated from strain rate and stress using the relationship

$$\eta = \sigma/\dot{\varepsilon}$$

to calculate viscosity from olivine water concentrations, the temperature, pressure, and stress of deformation must be known. Spinel peridotites lack good geobarometers, but pressure at shallow depths has a negligible effect on viscosity as activation volume is small. In orogenic and abyssal peridotites, emplacement is slow and temperatures recovered using geothermometers usually record reequilibration to temperatures a few hundred degrees below the melting temperature. Therefore, instead of using thermobarometry to estimate the pressure-temperature conditions at which each peridotite last equilibrated, effective viscosity (Table 6) was calculated for all samples using a temperature of 1250°C, depth of ~15 km (0.5 GPa), and stress of 0.3 MPa. Comparison at these conditions is equivalent to the viscosity within the lithosphere after melting.

Variations in effective viscosity among our samples and literature xenoliths are shown in Figure 12. For samples with <3 ppm H_2O (<50 ppm H/Si), their viscosity is that of dry dislocation creep, which has a value of 2.5×10^{21} Pa s at 1250°C and 0.5 GPa. The viscosity of the most water-rich sample in this study, from the Josephine Peridotite, is 6×10^{19} Pa s, which is over an order of magnitude lower than the dry viscosity. Upper mantle viscosity is $6–30 \times 10^{19}$ Pa s, based on the *Hirschmann* [2006] estimate of 50–200 ppm H_2O in bulk upper mantle (i.e., premelting mantle). If these calculations are made at 1350°C and 100 km (3.3 GPa), which roughly corresponds to the lithosphere-asthenosphere boundary, then predicted viscosities decrease: Nominally dry samples are 2×10^{21} Pa s, while the wettest sample is 1.5×10^{19} Pa s.

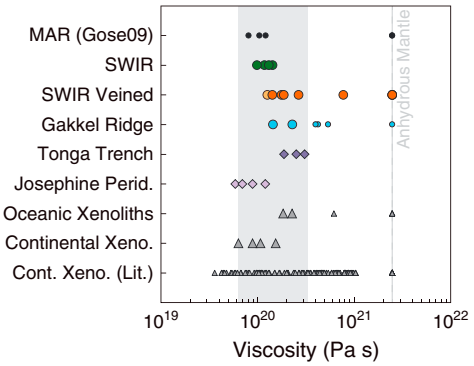

Figure 12. Range of effective mantle viscosities (Table 6), calculated at a temperature of 1250°C, pressure of 0.5 GPa (~15 km), and shear stress of 0.3 MPa. The dislocation creep flow law for wet olivine as a function of C_{OH} [*Hirth and Kohlstedt*, 2003] was used, combined with modeled olivine water concentrations (Table 6). At water contents <3 ppm H_2O (<50 ppm H/Si), the flow law for dry olivine was used to calculate viscosity, as creep rate is no longer controlled by the charge neutrality condition [*Mei and Kohlstedt*, 2000]. The grey shaded box is the estimated viscosity range for the upper mantle based on the *Hirschmann* [2006] estimate for upper mantle water contents of 8–32 ppm H_2O (130–520 ppm H/Si) in olivine.

6. Discussion of Phosphorus in Peridotites

This study provides preliminary constraints on the concentration of P in peridotite minerals following melting, based on the analysis of P in Pali Aike xenoliths and SWIR pyroxenite-veined peridotites. The Pali Aike xenoliths have an average P concentration of 48 ppm in olivine, 7 ppm in Opx, and 25 ppm in Cpx. The concentration of P in the pyroxenite-veined peridotites ranges from 1 to 15 ppm in Opx and 5 to 29 ppm in Cpx (Figure 3). Extensive literature data do not exist for P in mantle peridotites. Limited measurements by laser ablation inductively coupled plasma mass spectrometry have found that P ranges from 5 to 79 ppm in olivine, 16 to 40 ppm in Opx, and 9 to 148 ppm in Cpx [e.g., *Witt-Eickschen and O'Neill*, 2005; *Mallmann et al*., 2009; *De Hoog et al*., 2010]. These studies include xenoliths with a range of compositions, from spinel and garnet lherzolites to amphibole-bearing harzburgites.

Our results indicate that P is more compatible in olivine than in pyroxenes, as $D_P^{Ol/Opx} = 8\pm2$, $D_P^{Ol/Cpx} = 1.9\pm0.2$, and $D_P^{Cpx/Opx} = 3\pm1$. These values broadly agree with previous xenolith data ($D_P^{Ol/Opx} = 2\pm2$, $D_P^{Ol/Cpx} = 1.0\pm0.1$, and $D_P^{Cpx/Opx} = 2\pm1$), given analytical uncertainties. Substitution of P into silicates can occur by the charge-coupled substitution $2Si^{4+} = P^{5+} + Al^{3+}$, but such a mechanism cannot explain the preference of P for olivine over Al-bearing pyroxenes. Recent experimental work by *Grant and Kohn* [2013] has shown that the incorporation of P into olivine is not dependent on Al. Instead, they found that P substitutes for Si in olivine and is charge balanced by these vacancies, implying that $D_P^{Ol/Opx}$ is controlled by the energetics of producing these vacancies. Clearly, more measurements of P in peridotites are necessary to better understand the behavior of this volatile element in the mantle.

7. Discussion of Fluorine in Peridotites

Results from this study also provide constraints on the behavior of F in peridotites. Concentrations of F range from 0.02 to 2 ppm in olivine, from 0.1 to 26 ppm in Opx, and from 0.1 to 66 ppm in Cpx (Figure 3). These values are in agreement with the range measured by *Mosenfelder and Rossman* [2013a, 2013b] for mantle xenoliths. Fluorine concentrations probably extend to lower values, as several samples were below detection. Converted to bulk rock concentrations, our samples have bulk F concentrations of 0.1–18 ppm. For comparison, the estimated concentration of F in the upper mantle is 11 ± 5 ppm [*Salters and Stracke*, 2004] and in bulk silicate Earth is 25 ppm [*McDonough and Sun*, 1995]. Samples with concentrations >11 ppm are Pali Aike xenoliths and SWIR pyroxenite veins, which are not necessarily expected to have low concentrations. In contrast, the amount of F in residual SWIR peridotites is <11 ppm, confirming that F is incompatible during melting.

Based on this study, F partition coefficients are $D_F^{Ol/Opx} = 0.06\pm0.05$ ($N = 5$), $D_F^{Ol/Cpx} = 0.02\pm0.02$ ($N = 4$), and $D_F^{Cpx/Opx} = 3.5\pm1$ ($N = 17$). A single experimental estimate of $D_F^{Ol/Opx} = 0.11\pm0.02$ from *Beyer et al*. [2012] provides a comparison. The value for $D_F^{Cpx/Opx}$ is reasonably robust, but the low concentration of F in olivine and the small number of olivine analyses means that more data are necessary to improve estimates of $D_F^{Ol/Opx}$ and $D_F^{Ol/Cpx}$. Despite this, existing data indicate that the order of relative F compatibility is Cpx > Opx > Ol, which is the same order as for H_2O, but different than for P.

Several studies have suggested that F substitutes into NAMs via the same mechanisms as hydrogen [*Hervig and Bell*, 2005; *Guggino et al*., 2007; *Bromiley and Kohn*, 2007; *O'Leary et al*., 2010; *Mosenfelder et al*., 2011; *Beyer et al*., 2012; *Dalou et al*., 2012; *Mosenfelder and Rossman*, 2013a, 2013b]. However, fluorine is also proposed to behave similarly to phosphorous during mantle melting [*Schilling et al*., 1980; *Saal et al*., 2002], with the relatively constant F/P ratio of MORBs being used to constrain upper mantle P (41 ppm) [*Salters and Stracke*, 2004]. This observation is surprising given that olivine is the main mantle host for P, whereas Cpx is the main host for F. Hence, more studies of F in peridotites and melts are necessary to constrain the amount of F in the mantle, particularly as recent work [e.g., *Bromiley and Kohn*, 2007; *Beyer et al*., 2012; *Mosenfelder and Rossman*, 2013a, 2013b] suggests that NAMs may control the mantle F budget.

If F and H_2O in olivine are correlated, then F contents in olivine could be used to calculate olivine H_2O concentrations. This type of analysis would provide confirmation of olivine H_2O concentrations calculated from pyroxene H_2O concentrations. More data for F and H_2O in undegassed olivines are necessary for this type of analysis to be possible.

8. Conclusions

This study presents data for volatile (H_2O, P, and F) concentrations in olivine, orthopyroxene, and clinopyroxene from abyssal, orogenic, and xenolith peridotites. Our results demonstrate that pyroxenes can be used to constrain upper mantle water concentrations but that olivines in orogenic and abyssal peridotites have diffusively lost water. At high levels of alteration, pyroxenes show evidence for water enrichment, but this can largely be avoided by petrographic characterization of samples prior to analysis. If the partition coefficient $D_{H_2O}^{Ol/Opx}$ or $D_{H_2O}^{Ol/Cpx}$ is known, the amount of water in upper mantle olivines can be determined from the water content of coexisting pyroxenes. The bulk water concentration for peridotites can then be calculated using mineral modes. Hence, the analysis of water in pyroxenes provides a powerful tool for investigating the role of water in upper mantle processes, such as melting and deformation.

The amount of water in Cpx in this study ranges from 60 to 670 ppm, with the lowest concentration occurring in an abyssal pyroxenite vein and the highest concentration in a Pali Aike xenolith. Opx ranges from 10 to 300 ppm, with the lowest water concentration also occurring in an abyssal pyroxenite vein and the highest concentration in a deformed Josephine peridotite. The average Cpx/Opx partition coefficient in this study is in close agreement with published xenolith values, which combined have a value of $D_{H_2O}^{Cpx/Opx} = 2.6\pm0.9$ (152 samples). However, natural samples are systematically offset from published experimental values ($D_{H_2O}^{Cpx/Opx} = 1.3\pm0.3$, 10 experiments). Possible causes for this offset include differences in composition, total water content, temperature, and oxygen fugacity.

Olivine concentrations are calculated based on Opx water concentrations and using the experimental estimate of $D_{H_2O}^{Ol/Opx} = 0.11\pm0.03$, which gives an olivine concentration range of 1–34 ppm H_2O (16–550 ppm H/Si). Lithospheric effective viscosity, calculated from these olivine water concentrations and the dislocation creep flow law, is 6×10^{19} Pa s at 1250°C and 15 km depth for the most water-rich peridotite, compared to a dry effective viscosity of 2.5×10^{21} Pa s. At 1350°C and 100 km, the viscosity of the wettest peridotite is reduced to 1.5×10^{19} Pa s, compared to a dry viscosity of 2×10^{21} Pa s.

Calculated bulk rock water concentrations are 20–220 ppm, estimated using mineral concentrations and modes. Among abyssal peridotites, these concentrations are correlated with Cpx mode, bulk Al_2O_3, bulk Ce, and spinel Cr#, all of which are proxies for degree of melting. However, while modeling of fractional melting can reproduce observed REE patterns for ridge peridotites, it cannot reproduce the water contents. Abyssal peridotites thus appear to have higher water concentrations than expected for the residues of melting. One possible explanation for this is the addition of water by late-stage melt percolation, occurring at temperatures too low for other elements to diffusively equilibrate. Pyroxenites and pyroxenite-veined peridotites associated with Bouvet hot spot have very low water contents and are best explained by the presence of recycled dehydrated oceanic crust in the plume source.

Phosphorous, which was only measured in a few samples, is more compatible in olivine than in pyroxenes, with concentrations of 50 ppm in olivine, 1–15 ppm in Opx, and 5–29 ppm in Cpx. Fluorine concentrations are 0.02–2 ppm in olivine, 0.1–26 ppm in Opx, and 0.1–66 ppm in Cpx. Calculated bulk F

concentrations using mineral modes give a range of 0.1–18 ppm. Fluorine demonstrates similar partitioning behavior to H_2O in peridotites, but with lower concentrations. If F substitutes into olivine via the same mechanisms as H^+, then it could be possible to determine original water contents in olivine based on F concentrations.

Acknowledgments
J. Wang is thanked for assistance with the SIMS analyses. C. MacLeod and H. Dick generously provided some of the abyssal peridotite samples. We thank S. Demouchy, G. Gaetani, M. Hirschmann, G. Hirth, C. Holyoke, J. O'Leary, P. Skemer, and E. Stolper for useful discussions. S. Kohn, T. Tenner, and H. Skogby gave insightful reviews and M. Walter provided thoughtful editorial handling. All new data presented in this paper are available in the seven tables and four supplemental tables. This study was supported by the Carnegie Institution of Washington and by NSF grant EAR-1255620 to J.M.W.

References

Alt, J. C., W. C. Shanks, W. Bach, H. Paulick, C. J. Garrido, and G. Beaudoin (2007), Hydrothermal alteration and microbial sulfate reduction in peridotite and gabbro exposed by detachment faulting at the Mid-Atlantic Ridge, 15°20'N (ODP Leg 209): A sulfur and oxygen isotope study, *Geochem. Geophys. Geosyst.*, *8*, Q08002, doi:10.1029/2007GC001617.

Amundsen, H. E. F., W. L. Griffin, and S. Y. O'Reilly (1987), The lower crust and upper mantle beneath northwestern Spitsbergen: Evidence from xenoliths and geophysics, *Tectonophysics*, *139*, 169–185.

Anders, E., and N. Grevesse (1989), Abundances of the elements: Meteoritic and solar, *Geochim. Cosmochim. Acta*, *53*(1), 197–214.

Andrut, M., F. Brandstätter, and A. Beran (2003), Trace hydrogen zoning in diopside, *Mineral. Petrol.*, *78*, 231–241.

Arai, S., and S. Ishimaru (2007), Insights into petrological characteristics of the lithosphere of mantle wedge beneath arcs through peridotite xenoliths: A review, *J. Petrol.*, *49*(4), 665–695, doi:10.1093/petrology/egm069.

Ardia, P., M. M. Hirschmann, A. C. Withers, and T. J. Tenner (2012), H_2O storage capacity of olivine at 5–8 GPa and consequences for dehydration partial melting of the upper mantle, *Earth Planet. Sci. Lett.*, *345-348*, 104–116.

Asimow, P. D., J. E. Dixon, and C. H. Langmuir (2004), A hydrous melting and fractionation model for mid-ocean ridge basalts: Application to the Mid-Atlantic Ridge near the Azores, *Geochem. Geophys. Geosyst.*, *5*, Q01E16, doi:10.1029/2003GC000568.

Aubaud, C., E. H. Hauri, and M. M. Hirschmann (2004), Hydrogen partition coefficients between nominally anhydrous minerals and basaltic melts, *Geophys. Res. Lett.*, *31*, L20611, doi:10.1029/2004GL021341.

Aubaud, C., A. C. Withers, M. M. Hirschmann, Y. Guan, L. A. Leshin, S. J. Mackwell, and D. R. Bell (2007), Intercalibration of FTIR and SIMS for hydrogen measurements in glasses and nominally anhydrous minerals, *Am. Mineral.*, *92*(5-6), 811–828, doi:10.2138/am.2007.2248.

Aubaud, C., M. M. Hirschmann, A. C. Withers, and R. L. Hervig (2008), Hydrogen partitioning between melt, clinopyroxene, and garnet at 3 GPa in a hydrous MORB with 6 wt.% H_2O, *Contrib. Mineral. Petrol.*, *156*(5), 607–625.

Aubaud, C., H. Bureau, C. Raepsaet, H. Khodja, A. C. Withers, M. M. Hirschmann, and D. R. Bell (2009), Calibration of the infrared molar absorption coefficients for H in olivine, clinopyroxene and rhyolitic glass by elastic recoil detection analysis, *Chem. Geol.*, *262*(1-2), 78–86, doi:10.1016/j.chemgeo.2009.01.001.

Bach, W., and F. Klein (2009), The petrology of seafloor rodingites: Insights from geochemical reaction path modeling, *Lithos*, *112*(1-2), 103–117, doi:10.1016/j.lithos.2008.10.022.

Bach, W., C. J. Garrido, H. Paulick, J. Harvey, and M. Rosner (2004), Seawater-peridotite interactions: First insights from ODP Leg 209, MAR 15°N, *Geochem. Geophys. Geosyst.*, *5*, Q09F26, doi:10.1029/2004GC000744.

Bell, D. R., and G. R. Rossman (1992), Water in Earth's mantle: The role of nominally anhydrous minerals, *Science*, *255*(5050), 1391–1397.

Bell, D. R., G. R. Rossman, J. Maldener, D. Endisch, and F. Rauch (2003), Hydroxide in olivine: A quantitative determination of the absolute amount and calibration of the IR spectrum, *J. Geophys. Res.*, *108*(B2), 2105, doi:10.1029/2001JB000679.

Beyer, C., S. Klemme, M. Wiedenbeck, A. Stracke, and C. Vollmer (2012), Fluorine in nominally fluorine-free mantle minerals: Experimental partitioning of F between olivine, orthopyroxene and silicate melts with implications for magmatic processes, *Earth Planet. Sci. Lett.*, *337-338*, 1–9, doi:10.1016/j.epsl.2012.05.003.

Bloomer, S. H., and R. L. Fisher (1987), Petrology and geochemistry of igneous rocks from the Tonga Trench—A non-accreting plate boundary, *J. Geol.*, *95*, 469–495.

Bonadiman, C., Y. Hao, M. Coltorti, L. Dallai, B. Faccini, Y. Huang, and Q.-K. Xia (2009), Water contents of pyroxenes in intraplate lithospheric mantle, *Eur. J. Mineral.*, *21*(3), 637–647.

Bromiley, D. W., and S. C. Kohn (2007), Comparisons between fluoride and hydroxide incorporation in nominally anhydrous and fluorine-free mantle minerals, *Goldschmidt Conf. Abstr.*, *71*, A124.

Carpenter, S. (2003), The kinetics of hydrogen diffusion in single crystal orthopyroxene, PhD thesis, Pennsylvania State University.

Cherniak, D. J., and A. Dimanov (2010), Diffusion in pyroxene, mica and amphibole, *Rev. Mineral. Geochem.*, *72*, 641–690, doi:10.2138/rmg.2010.72.14.

Cherniak, D. J., and Y. Liang (2007), Rare earth element diffusion in natural enstatite, *Geochim. Cosmochim. Acta*, *71*(5), 1324–1340, doi:10.1016/j.gca.2006.12.001.

Craddock, P. R., J. M. Warren, and N. Dauphas (2013), Abyssal peridotites reveal the near-chondritic Fe isotopic composition of the Earth, *Earth Planet. Sci. Lett.*, *365*, 63–76, doi:10.1016/j.epsl.2013.01.011.

Dai, L., and S.-I. Karato (2009), Electrical conductivity of orthopyroxene: Implications for the water content of the asthenosphere, *Proc. Jpn. Acad. Ser. B*, *85*(10), 466–475, doi:10.2183/pjab.85.466.

Dalou, C., K. T. Koga, N. Shimizu, J. Boulon, and J.-L. Devidal (2012), Experimental determination of F and Cl partitioning between lherzolite and basaltic melt, *Contrib. Mineral. Petrol.*, *163*(4), 591–609, doi:10.1007/s00410-011-0688-2.

De Hoog, J. C. M., L. Gall, and D. H. Cornell (2010), Trace-element geochemistry of mantle olivine and application to mantle petrogenesis and geothermobarometry, *Chem. Geol.*, *270*(1-4), 196–215, doi:10.1016/j.chemgeo.2009.11.017.

Demouchy, S., and S. J. Mackwell (2006), Mechanisms of hydrogen incorporation and diffusion in iron-bearing olivine, *Phys. Chem. Miner.*, *33*(5), 347–355, doi:10.1007/s00269-006-0081-2.

Demouchy, S., S. D. Jacobsen, F. Gaillard, and C. R. Stern (2006), Rapid magma ascent recorded by water diffusion profiles in mantle olivine, *Geology*, *34*(6), 429–432, doi:10.1130/G22386.1.

Denis, C. M. M., S. Demouchy, and C. S. J. Shaw (2013), Evidence of dehydration in peridotites from Eifel Volcanic Field and estimates of the rate of magma ascent, *J. Volcanol. Geotherm. Res.*, *258*, 85–99.

Dick, H. J. B. (1976), Origin and emplacement of the Josephine Peridotite of southwestern Oregon, PhD thesis, Yale University.

Dixon, J. E., L. Leist, C. H. Langmuir, and J.-G. Schilling (2002), Recycled dehydrated lithosphere observed in plume-influenced mid-ocean-ridge basalt, *Nature*, *420*, 385–389.

Dyar, M. D., A. V. McGuire, and R. D. Ziegler (1989), Redox equilibria and crystal chemistry of coexisting minerals from spinel lherzolite mantle xenoliths, *Am. Mineral.*, *74*(9-10), 969–980.

Eggins, S. M., R. L. Rudnick, and W. F. McDonough (1998), The composition of peridotites and their minerals: A laser-ablation ICP-MS study, *Earth Planet. Sci. Lett.*, *154*, 53–71.
Falus, G., A. Tommasi, J. Ingrin, and C. Szabo (2008), Deformation and seismic anisotropy of the lithospheric mantle in the southeastern Carpathians inferred from the study of mantle xenoliths, *Earth Planet. Sci. Lett.*, *272*(1-2), 50–64, doi:10.1016/j.epsl.2008.04.035.
Farver, J. R. (2010), Oxygen and hydrogen diffusion in minerals, *Rev. Mineral. Geochem.*, *72*, 447–507, doi:10.2138/rmg.2010.72.10.
Fisher, R. L., and C. G. Engel (1969), Ultramafic and basaltic rocks dredged from the nearshore flank of the Tonga trench, *Bull. Geol. Soc. Am.*, *80*, 1373–1378.
Godard, M., J.-L. Bodinier, and G. Vasseur (1995), Effects of mineralogical reactions on trace element redistributions in mantle rocks during percolation processes: A chromatographic approach, *Earth Planet. Sci. Lett.*, *133*, 449–461.
Godard, M., Y. Lagabrielle, O. Alard, and J. Harvey (2008), Geochemistry of the highly depleted peridotites drilled at ODP Sites 1272 and 1274 (Fifteen-Twenty Fracture Zone, Mid-Atlantic Ridge): Implications for mantle dynamics beneath a slow spreading ridge, *Earth Planet. Sci. Lett.*, *267*(3-4), 410–425, doi:10.1016/j.epsl.2007.11.058.
Goetze, C., and D. L. Kohlstedt (1973), Laboratory study of dislocation climb and diffusion in olivine, *J. Geophys. Res.*, *78*(26), 5961–5971.
Gose, J., E. Schmädicke, and A. Beran (2009), Water in enstatite from Mid-Atlantic Ridge peridotite: Evidence for the water content of suboceanic mantle?, *Geology*, *37*(6), 543–546.
Gose, J., E. Schmädicke, and R. Stalder (2011), Water in mantle orthopyroxene—No visible change in defect water during serpentinization, *Eur. J. Mineral.*, *23*(4), 529–536, doi:10.1127/0935-1221/2011/0023-2122.
Grant, T. B., and S. C. Kohn (2013), Phosphorus partitioning between olivine and melt: An experimental study in the system Mg_2SiO_4-$Ca_2Al_2Si_2O_9$-$NaAlSi_3O_8$-$Mg_3(PO_4)_2$, *Am. Mineral.*, *98*, 1860–1869.
Grant, K. J., S. C. Kohn, and R. A. Brooker (2006), Solubility and partitioning of water in synthetic forsterite and enstatite in the system MgO–SiO_2–$H_2O \pm Al_2O_3$, *Contrib. Mineral. Petrol.*, *151*(6), 651–664.
Grant, K. J., J. Ingrin, J.-P. Lorand, and P. Dumas (2007a), Water partitioning between mantle minerals from peridotite xenoliths, *Contrib. Mineral. Petrol.*, *154*(1), 15–34, doi:10.1007/s00410-006-0177-1.
Grant, K. J., S. C. Kohn, and R. A. Brooker (2007b), The partitioning of water between olivine, orthopyroxene and melt synthesised in the system albite-forsterite-H_2O, *Earth Planet. Sci. Lett.*, *260*(1-2), 227–241.
Guggino, S. N., R. L. Hervig, and D. R. Bell (2007), Fluorine in olivines from plutonic, extrusive, and hypabyssal suites, *Eos Trans. AGU*, *88*(52), V41B–0609.
Harper, G. D. (1984), The Josephine ophiolite, northwestern California, *Geol. Soc. Am. Bull.*, *95*(9), 1009–1026.
Hart, S. R., and T. Dunn (1993), Experimental cpx/melt partitioning of 24 trace elements, *Contrib, Mineral. Petrol.*, *113*(1), 1–8.
Hauri, E. H., and S. R. Hart (1994), Constraints on melt migration from mantle plumes: A trace element study of peridotite xenoliths from Savai'i, Western Samoa, *J. Geophys. Res.*, *99*(B12), 24–301–24–321.
Hauri, E. H., N. Shimizu, J. J. Dieu, and S. R. Hart (1993), Evidence for hotspot-related carbonatite metasomatism in the oceanic upper mantle, *Nature*, *365*, 221–227.
Hauri, E. H., J. Wang, J. E. Dixon, P. L. King, C. Mandeville, and S. Newman (2002), SIMS analysis of volatiles in silicate glasses 1. Calibration, matrix effects and comparisons with FTIR, *Chem. Geol.*, *183*, 99–114.
Hauri, E. H., G. A. Gaetani, and T. H. Green (2006), Partitioning of water during melting of the Earth's upper mantle at H_2O-undersaturated conditions, *Earth Planet. Sci. Lett.*, *248*, 715–734, doi:10.1016/j.epsl.2006.06.014.
Hellebrand, E., J. E. Snow, P. Hoppe, and A. W. Hofmann (2002), Garnet-field melting and late-stage refertilization in "residual" abyssal peridotites from the Central Indian Ridge, *J. Petrol.*, *43*(12), 2305–2338.
Hercule, S., and J. Ingrin (1999), Hydrogen in diopside: Diffusion, kinetics of extraction-incorporation, and solubility, *Am. Mineral.*, *84*, 15,77–15,87.
Hervig, R. L., and D. R. Bell (2005), Fluorine and hydrogen in mantle megacrysts, *AGU Fall Meet. Abstr.*, *41*, V41A–1426.
Hirschmann, M. M. (2006), Water, melting, and the deep Earth H_2O cycle, *Annu. Rev. Earth Planet. Sci.*, *34*, 627–653.
Hirschmann, M. M., T. J. Tenner, C. Aubaud, and A. C. Withers (2009), Dehydration melting of nominally anhydrous mantle: The primacy of partitioning, PEPI, *176*(1–2), 54–68.
Hirth, G., and D. L. Kohlstedt (1995), Experimental constraints on the dynamics of the partially molten upper mantle 2. Deformation in the dislocation creep regime, *J. Geophys. Res.*, *100*(B8), 15,441–15,449.
Hirth, G., and D. L. Kohlstedt (1996), Water in the oceanic upper mantle: Implications for rheology, melt extraction and the evolution of the lithosphere, *Earth Planet. Sci. Lett.*, *144*(1-2), 93–108.
Hirth, G., and D. L. Kohlstedt (2003), Rheology of the upper mantle and the mantle wedge: A view from the experimentalists, *Geophys. Monogr.*, *138*, 83–105.
Ingrin, J., and M. Blanchard (2006), Diffusion of hydrogen in minerals, *Rev. Mineral. Geochem.*, *62*, 291–320.
Ingrin, J., and H. Skogby (2000), Hydrogen in nominally anhydrous upper-mantle minerals: Concentration levels and implications, *Eur. J. Mineral.*, *12*, 543–570.
Ingrin, J., S. Hercule, and T. Charton (1995), Diffusion of hydrogen in diopside: Results of dehydration experiments, *J. Geophys. Res.*, *100*(B8), 15,489–15,499.
Ionov, D. A., C. Dupuy, S. Y. O'Reilly, M. G. Kopylova, and Y. S. Genshaft (1993), Carbonated peridotite xenoliths from Spitsbergen: Implications for trace element signature of mantle carbonate metasomatism, *Earth Planet. Sci. Lett.*, *119*(3), 283–297.
Ionov, D. A., S. Y. O'Reilly, Y. S. Genshaft, and M. G. Kopylova (1996), Carbonate-bearing mantle peridotite xenoliths from Spitsbergen: Phase relationships, mineral compositions and trace-element residence, *Contrib. Mineral. Petrol.*, *125*(4), 375–392.
Irving, A. J., and F. A. Frey (1984), Trace element abundances in megacrysts and their host basalts: Constraints on partition coefficients and megacryst genesis, *Geochim. Cosmochim. Acta*, *48*, 1201–1221.
Jung, H., and S.-I. Karato (2001), Water-Induced Fabric Transitions in Olivine, *Science*, *293*, 1460–1463.
Jung, H., I. Katayama, Z. Jiang, T. Hiraga, and S.-I. Karato (2006), Effect of water and stress on the lattice-preferred orientation of olivine, *Tectonophysics*, *421*, 1–22, doi:10.1016/j.tecto.2006.02.011.
Karato, S.-I. (2008), *Deformation of Earth Materials*, Cambridge Univ. Press, Cambridge.
Karato, S.-I., M. S. Paterson, and J. D. Fitz Gerald (1986), Rheology of synthetic olivine aggregates: Influence of grain size and water, *J. Geophys. Res.*, *91*(B8), 8151–8176.
Kelemen, P. B., and H. J. B. Dick (1995), Focused melt flow and localized deformation in the upper mantle: Juxtaposition of replacive dunite and ductile shear zones in the Josephine peridotite, SW Oregon, *J. Geophys. Res.*, *100*(B1), 423–438.
Kelemen, P. B., N. Shimizu, and V. J. M. Salters (1995), Extraction of mid-ocean-ridge basalt from the upwelling mantle by focused flow of melt in dunite channels, *Nature*, *375*, 747–753.

Kelemen, P. B., G. M. Yogodzinski, and D. W. Scholl (2003), Along-strike variation in the Aleutian island arc: Genesis of high Mg# andesite and implications for continental crust, in *The Subduction Factory*, *Geophys. Monogr. Ser.*, vol. 138, edited by J. Eiler, pp. 223–276, AGU, Washington, D. C.

Keppler, H., and N. Bolfan-Casanova (2006), Thermodynamics of water solubility and partitioning, *Rev. Mineral. Geochem.*, *62*, 193–230.

Kinzler, R. J. (1997), Melting of mantle peridotite at pressures approaching the spinel to garnet transition: Application to mid-ocean ridge basalt petrogenesis, *J. Geophys. Res.*, *102*(B1), 853–874.

Klein, F., W. Bach, N. Jöns, T. M. McCollom, B. Moskowitz, and T. Berquó (2009), Iron partitioning and hydrogen generation during serpentinization of abyssal peridotites from 15°N on the Mid-Atlantic Ridge, *Geochim. Cosmochim. Acta*, *73*, 6868–6893, doi:10.1016/j.gca.2009.08.021.

Kneller, E. A., P. E. van Keken, S.-I. Karato, and J. Park (2005), B-type olivine fabric in the mantle wedge: Insights from high-resolution non-Newtonian subduction zone models, *Earth Planet. Sci. Lett.*, *237*, 781–797.

Koga, K. T., E. H. Hauri, M. M. Hirschmann, and D. R. Bell (2003), Hydrogen concentration analyses using SIMS and FTIR: Comparison and calibration for nominally anhydrous minerals, *Geochem. Geophys. Geosyst.*, *4*(2), Q01019, doi:10.1029/2002GC000378.

Kohlstedt, D. L., and S. J. Mackwell (1998), Diffusion of hydrogen and intrinsic point defects in olivine, *Z. Phys. Chem.*, *207*, 147–162.

Kohlstedt, D. L., and S. J. Mackwell (1999), Solubility and diffusion of "water" in silicate minerals, in *Microscopic Properties and Processes in Minerals*, edited by K. Wright and R. Catlow, pp. 539–559, Kluwer Academic Publishers, Dordrecht, Netherlands.

Kohn, S. C., and K. J. Grant (2006), The partitioning of water between nominally anhydrous minerals and silicate melts, *Rev. Mineral. Geochem.*, *62*, 231–241.

Kohn, S. C., B. M. Roome, M. E. Smith, and A. P. Howes (2005), Testing a potential mantle geohygrometer; the effect of dissolved water on the intracrystalline partitioning of Al in orthopyroxene, *Earth Planet. Sci. Lett.*, *238*, 342–350.

Kovács, I., H. S. C. O'Neill, J. Hermann, and E. H. Hauri (2010), Site-specific infrared O-H absorption coefficients for water substitution into olivine, *Am. Mineral.*, *95*(2-3), 292–299, doi:10.2138/am.2010.3313.

le Roux, P. J., S. B. Shirey, E. H. Hauri, M. R. Perfit, and J. F. Bender (2006), The effects of variable sources, processes and contaminants on the composition of northern EPR MORB (8-10°N and 12-14°N): Evidence from volatiles (H_2O, CO_2, S) and halogens (F, Cl), *Earth Planet. Sci. Lett.*, *251*(3-4), 209–231, doi:10.1016/j.epsl.2006.09.012.

Li, Z.-X. A., C.-T. A. Lee, A. H. Peslier, A. Lenardic, and S. J. Mackwell (2008), Water contents in mantle xenoliths from the Colorado Plateau and vicinity: Implications for the mantle rheology and hydration-induced thinning of continental lithosphere, *J. Geophys. Res.*, *113*, B09210, doi:10.1029/2007JB005540.

Long, M. D., and P. G. Silver (2008), The subduction zone flow field from seismic anisotropy: A global view, *Science*, *319*(5861), 315–318.

Mackwell, S. J., and D. L. Kohlstedt (1990), Diffusion of hydrogen in olivine: Implications for water in the mantle, *J. Geophys. Res.*, *95*(B4), 5079–5088.

Mallmann, G., H. S. C. O'Neill, and S. Klemme (2009), Heterogeneous distribution of phosphorus in olivine from otherwise well-equilibrated spinel peridotite xenoliths and its implications for the mantle geochemistry of lithium, *Contrib. Mineral. Petrol.*, *158*(4), 485–504, doi:10.1007/s00410-009-0393-6.

McDonough, W. F., and S.-S. Sun (1995), The composition of the Earth, *Chem. Geol.*, *120*(3-4), 223–253.

Mei, S., and D. L. Kohlstedt (2000), Influence of water on plastic deformation of olivine aggregates: 2. Dislocation creep regime, *J. Geophys. Res.*, *105*(B9), 21,471–21,481, doi:10.1029/2000JB900180.

Michael, P. J. (1995), Regionally distinctive sources of depleted MORB: Evidence from trace elements and H2O, *Earth Planet. Sci. Lett.*, *131*, 301–320.

Michael, P. J., et al. (2003), Magmatic and amagmatic seafloor generation at the ultraslow-spreading Gakkel ridge, Arctic Ocean, *Nature*, *423*, 956–961.

Mosenfelder, J. L., and G. R. Rossman (2013a), Analysis of hydrogen and fluorine in pyroxenes: I. Orthopyroxene, *Am. Mineral.*, *98*(5-6), 1026–1041, doi:10.2138/am.2013.4291.

Mosenfelder, J. L., and G. R. Rossman (2013b), Analysis of hydrogen and fluorine in pyroxenes: II. Clinopyroxene, *Am. Mineral.*, *98*(5-6), 1042–1054, doi:10.2138/am.2013.4413.

Mosenfelder, J. L., M. Le Voyer, G. R. Rossman, Y. Guan, D. R. Bell, P. D. Asimow, and J. M. Eiler (2011), Analysis of hydrogen in olivine by SIMS: Evaluation of standards and protocol, *Am. Mineral.*, *96*(11-12), 1725–1741, doi:10.2138/am.2011.3810.

Nadeau, S., P. Philippot, and F. C. C. O. Pineau (1993), Fluid inclusion and mineral isotopic compositions (HCO) in eclogitic rocks as tracers of local fluid migration during high-pressure metamorphism, *Earth Planet. Sci. Lett.*, *114*(4), 431–448, doi:10.1016/0012-821X(93)90074-J.

Nazzareni, S., H. Skogby, and P. F. Zanazzi (2011), Hydrogen content in clinopyroxene phenocrysts from Salina mafic lavas (Aeolian arc, Italy), *Contrib. Mineral. Petrol.*, *162*(2), 275–288, doi:10.1007/s00410-010-0594-z.

Norman, M. D. (1998), Melting and metasomatism in the continental lithosphere: Laser ablation ICPMS analysis of minerals in spinel lherzolites from eastern Australia, *Contrib. Mineral. Petrol.*, *130*(3), 240–255.

Ohuchi, T., T. Kawazoe, Y. Nishihara, and T. Irifune (2012), Change of olivine a-axis alignment induced by water: Origin of seismic anisotropy in subduction zones, *Earth Planet. Sci. Lett.*, *317-318*, 111–119, doi:10.1016/j.epsl.2011.11.022.

O'Leary, J. A., G. A. Gaetani, and E. H. Hauri (2010), The effect of tetrahedral Al^{3+} on the partitioning of water between clinopyroxene and silicate melt, *Earth Planet. Sci. Lett.*, *297*(1-2), 111–120, doi:10.1016/j.epsl.2010.06.011.

Ozawa, K., and N. Shimizu (1995), Open-system melting in the upper mantle: Constraints from the Hayachine-Miyamori ophiolite, northeastern Japan, *J. Geophys. Res.*, *100*(B11), 22,315–22,335.

Peslier, A. H. (2010), A review of water contents of nominally anhydrous natural minerals in the mantles of Earth, Mars and the Moon, *J. Volcanol. Geotherm. Res.*, *197*(1-4), 239–258, doi:10.1016/j.jvolgeores.2009.10.006.

Peslier, A. H., and J. F. Luhr (2006), Hydrogen loss from olivines in mantle xenoliths from Simcoe (USA) and Mexico: Mafic alkalic magma ascent rates and water budget of the sub-continental lithosphere, *Earth Planet. Sci. Lett.*, *242*, 302–319, doi:10.1016/j.epsl.2005.12.019.

Peslier, A. H., J. F. Luhr, and J. Post (2002), Low water contents in pyroxenes from spinel-peridotites of the oxidized, sub-arc mantle wedge, *Earth Planet. Sci. Lett.*, *201*, 69–86.

Peslier, A. H., A. B. Woodland, and J. A. Wolff (2008), Fast kimberlite ascent rates estimated from hydrogen diffusion profiles in xenolithic mantle olivines from southern Africa, *Geochim. Cosmochim. Acta*, *72*(11), 2711–2722, doi:10.1016/j.gca.2008.03.019.

Peslier, A. H., A. B. Woodland, D. R. Bell, M. Lazarov, and T. J. Lapen (2012), Metasomatic control of water contents in the Kaapvaal cratonic mantle, *Geochim. Cosmochim. Acta*, *97*, 213–246, doi:10.1016/j.gca.2012.08.028.

Rauch, M., and H. Keppler (2002), Water solubility in orthopyroxene, *Contrib. Mineral. Petrol.*, *143*(5), 525–536, doi:10.1007/s00410-002-0365-6.

Saal, A. E., E. H. Hauri, C. H. Langmuir, and M. R. Perfit (2002), Vapour undersaturation in primitive mid-ocean-ridge basalt and the volatile content of the Earth's upper mantle, *Nature*, *419*(6906), 451–455, doi:10.1038/nature01073.

Salters, V. J. M., and A. Stracke (2004), Composition of the depleted mantle, *Geochem. Geophys. Geosyst.*, *5*, Q05004, doi:10.1029/2003GC000597.
Schilling, J.-G., M. B. Bergeron, and R. Evans (1980), Halogens in the mantle beneath the North Atlantic, *Philos. Trans. R. Soc. London Ser. A Math. Phys. Eng. Sci.*, *297*(1), 147–176, doi:10.1098/rsta.1980.0208.
Schmädicke, E., J. Gose, and T. M. Will (2011), Heterogeneous mantle underneath the North Atlantic: Evidence from water in orthopyroxene, mineral composition and equilibrium conditions of spinel peridotite from different locations at the Mid-Atlantic Ridge, *Lithos*, *125*(1-2), 308–320, doi:10.1016/j.lithos.2011.02.014.
Shaw, A. M., M. D. Behn, S. E. Humphris, R. A. Sohn, and P. M. Gregg (2010), Deep pooling of low degree melts and volatile fluxes at the 85°E segment of the Gakkel Ridge: Evidence from olivine-hosted melt inclusions and glasses, *Earth Planet. Sci. Lett.*, *289*(3-4), 311–322, doi:10.1016/j.epsl.2009.11.018.
Skemer, P., J. M. Warren, P. B. Kelemen, and G. Hirth (2010), Microstructural and rheological evolution of a mantle shear zone, *J. Petrol.*, *51*(1-2), 43–53, doi:10.1093/petrology/egp057.
Skemer, P., J. M. Warren, L. N. Hansen, G. Hirth, and P. B. Kelemen (2013), The influence of water and LPO on the initiation and evolution of mantle shear zones, *Earth Planet. Sci. Lett.*, *375*, 222–233, doi:10.1016/j.epsl.2013.05.034.
Skogby, H. (2006), Water in natural mantle minerals I: Pyroxenes, *Rev. Mineral. Geochem.*, *62*(1), 155–167, doi:10.2138/rmg.2006.62.7.
Skogby, H., D. R. Bell, and G. R. Rossman (1990), Hydroxide in pyroxene: Variations in the natural environment, *Am. Mineral.*, *75*(7-8), 764–774.
Smith, G. P., D. A. Wiens, K. M. Fischer, L. M. Dorman, S. C. Webb, and J. A. Hildebrand (2001), A complex pattern of mantle flow in the Lau backarc, *Science*, *292*(5517), 713–716, doi:10.1126/science.1058763.
Stalder, R. (2004), Influence of Fe, Cr and Al on hydrogen incorporation in orthopyroxene, *Eur. J. Mineral.*, *16*(5), 703–711, doi:10.1127/0935-1221/2004/0016-0703.
Stalder, R., and H. Skogby (2002), Hydrogen incorporation in enstatite, *Eur. J. Mineral.*, *14*(6), 1139–1144.
Stalder, R., and H. Skogby (2003), Hydrogen diffusion in natural and synthetic orthopyroxene, *Phys. Chem. Miner.*, *30*(1), 12–19, doi:10.1007/s00269-002-0285-z.
Stalder, R., H. Purwin, and H. Skogby (2007), Influence of Fe on hydrogen diffusivity in orthopyroxene, *Eur. J. Mineral.*, *19*(6), 899–904, doi:10.1127/0935-1221/2007/0019-1780.
Stalder, R., F. Prechtel, and T. Ludwig (2012), No site-specific infrared absorption coefficients for OH-defects in pure enstatite, *Eur. J. Mineral.*, *24*, 465–470.
Standish, J. J. (2006), The influence of ridge geometry at the ultraslow-spreading Southwest Indian Ridge (9°–25°E): Basalt composition sensitivity to variations in source and process, PhD thesis, MIT/WHOI Joint Program.
Standish, J. J., H. J. B. Dick, P. J. Michael, W. G. Melson, and T. O'Hearn (2008), MORB generation beneath the ultraslow spreading Southwest Indian Ridge (9–25°E): Major element chemistry and the importance of process versus source, *Geochem. Geophys. Geosyst.*, *9*, Q05004, doi:10.1029/2008GC001959.
Stern, C. R., S. Saul, M. A. Skewes, and K. Futa (1989), Garnet peridotite xenoliths from the Pali-Aike alkali basalts of southernmost South America, *Geol. Soc. Aust. Spec. Publ.*, *14*, 735–744.
Stern, C. R., R. Kilian, B. Olker, E. H. Hauri, and T. K. Kyser (1999), Evidence from mantle xenoliths for relatively thin (100 km) continental lithosphere below the Phanerozoic crust of southernmost South America, *Lithos*, *48*(1-4), 217–235.
Sundvall, R., and H. Skogby (2010), Hydrogen defect saturation in natural pyroxene, *Phys. Chem. Miner.*, *38*(5), 335–344, doi:10.1007/s00269-010-0407-y.
Sundvall, R., and R. Stalder (2011), Water in upper mantle pyroxene megacrysts and xenocrysts: A survey study, *Am. Mineral.*, *96*(8-9), 1215–1227, doi:10.2138/am.2011.3641.
Sundvall, R., H. Skogby, and R. Stalder (2009), Dehydration-hydration mechanisms in synthetic Fe-poor diopside, *Eur. J. Mineral.*, *21*(1), 17–26, doi:10.1127/0935-1221/2009/0021-1880.
Tenner, T. J., M. M. Hirschmann, A. C. Withers, and R. L. Hervig (2009), Hydrogen partitioning between nominally anhydrous upper mantle minerals and melt between 3 and 5 GPa and applications to hydrous peridotite partial melting, *Chem. Geol.*, *262*(1-2), 42–56, doi:10.1016/j.chemgeo.2008.12.006.
Tenner, T. J., M. M. Hirschmann, A. C. Withers, and P. Ardia (2012), H_2O storage capacity of olivine and low-Ca pyroxene from 10 to 13 GPa: Consequences for dehydration melting above the transition zone, *Contrib. Mineral. Petrol.*, *163*, 297–316.
Van Orman, J. A., T. L. Grove, and N. Shimizu (2001), Rare earth element diffusion in diopside: Influence of temperature, pressure, and ionic radius, and an elastic model for diffusion in silicates, *Contrib. Mineral. Petrol.*, *141*(6), 687–703.
Vernières, J., M. Godard, and J.-L. Bodinier (1997), A plate model for the simulation of trace element fractionation during partial melting and magma transport in the Earth's upper mantle, *J. Geophys. Res.*, *102*(B11), 24,771–24,784.
Wade, J. A., T. Plank, E. H. Hauri, K. A. Kelley, K. Roggensack, and M. Zimmer (2008), Prediction of magmatic water contents via measurement of H_2O in clinopyroxene phenocrysts, *Geology*, *36*(10), 799–802, doi:10.1130/G24964A.1.
Warren, J. M. (2007), *Geochemical And Rheological Constraints on the Dynamics of the Oceanic Upper Mantle*, Massachusetts Institute of Technology and Woods Hole Oceanographic Institution, Woods Hole, Mass.
Warren, J. M., and S. B. Shirey (2012), Lead and osmium isotopic constraints on the oceanic mantle from single abyssal peridotite sulfides, *Earth Planet. Sci. Lett.*, *359-360*, 279–293, doi:10.1016/j.epsl.2012.09.055.
Warren, J. M., G. Hirth, and P. B. Kelemen (2008), Evolution of olivine lattice preferred orientation during simple shear in the mantle, *Earth Planet. Sci. Lett.*, *272*(3-4), 501–512, doi:10.1016/j.epsl.2008.03.063.
Warren, J. M., N. Shimizu, C. Sakaguchi, H. J. B. Dick, and E. Nakamura (2009), An assessment of upper mantle heterogeneity based on abyssal peridotite isotopic compositions, *J. Geophys. Res.*, *114*, B12203, doi:10.1029/2008JB006186.
Withers, A. C. (2013), On the use of unpolarized infrared spectroscopy for quantitative analysis of absorbing species in birefringent crystals, *Am. Mineral.*, *98*(4), 689–697, doi:10.2138/am.2013.4316.
Withers, A. C., and M. M. Hirschmann (2007), H_2O storage capacity of $MgSiO_3$ clinoenstatite at 8–13 GPa, 1,100–1,400°C, *Contrib. Mineral. Petrol.*, *154*, 663–674.
Withers, A. C., M. M. Hirschmann, and T. J. Tenner (2011), The effect of Fe on olivine H_2O storage capacity: Consequences for H_2O in the Martian mantle, *Am. Mineral.*, *96*(7), 1039–1053, doi:10.2138/am.2011.3669.
Withers, A. C., H. Bureau, C. Raepsaet, and M. M. Hirschmann (2012), Calibration of infrared spectroscopy by elastic recoil detection analysis of H in synthetic olivine, *Chem. Geol.*, *334*, 92–98.
Witt-Eickschen, G., and H. S. C. O'Neill (2005), The effect of temperature on the equilibrium distribution of trace elements between clinopyroxene, orthopyroxene, olivine and spinel in upper mantle peridotite, *Chem. Geol.*, *221*(1-2), 65–101, doi:10.1016/j.chemgeo.2005.04.005.
Wood, B. J., L. T. Bryndzia, and K. E. Johnson (1990), Mantle oxidation state and its relationship to tectonic environment and fluid speciation, *Science*, *248*(4953), 337–345.

Woods, S. C., S. J. Mackwell, and M. D. Dyar (2000), Hydrogen in diopside: Diffusion profiles, *Am. Mineral.*, *85*(3-4), 480–487.
Workman, R. K., and S. R. Hart (2005), Major and trace element composition of the depleted MORB mantle (DMM), *Earth Planet. Sci. Lett.*, *231*(1-2), 53–72, doi:10.1016/j.epsl.2004.12.005.
Wright, D. J., S. H. Bloomer, C. J. MacLeod, B. Taylor, and A. M. Goodlife (2000), Bathymetry of the Tonga trench and forearc: A map series, *Mar. Geophys. Res.*, *21*, 489–511.
Xia, Q.-K., Y. Hao, P. Li, E. Deloule, M. Coltorti, L. Dallai, X.-Z. Yang, and M. Feng (2010), Low water content of the Cenozoic lithospheric mantle beneath the eastern part of the North China Craton, *J. Geophys. Res.*, *115*, B07207, doi:10.1029/2009JB006694.
Yang, X.-Z., Q.-K. Xia, E. Deloule, L. Dallai, Q.-C. Fan, and M. Feng (2008), Water in minerals of the continental lithospheric mantle and overlying lower crust: A comparative study of peridotite and granulite xenoliths from the North China Craton, *Chem. Geol.*, *256*(1-2), 33–45.
Yu, Y., X.-S. Xu, W. L. Griffin, S. Y. O'Reilly, and Q.-K. Xia (2011), H_2O contents and their modification in the Cenozoic subcontinental lithospheric mantle beneath the Cathaysia block, SE China, *Lithos*, *126*, 182–197.
Zou, H. (1998), Trace element fractionation during modal and nonmodal dynamic melting and open-system melting: A mathematical treatment, *Geochim. Cosmochim. Acta*, *62*(11), 1937–1945.